GROWTH AND CHARACTERIZATION OF MOLYBDENUM-BASED OXIDE
THIN FILM BY RF MAGNETRON SPUTTERING

by

NESLİHAN ŞİŞMAN

A Dissertation

Submitted to the Graduate School of Engineering and Natural Sciences

in partial fulfillment of the requirements for the degree of Master of Science.

Sabancı University

Fall 2022

ABSTRACT

GROWTH AND CHARACTERIZATION OF MOLYBDENUM-BASED OXIDE THIN FILM BY RF MAGNETRON SPUTTERING

Neslihan ŞİŞMAN

Materials Science and Nano Engineering, MSc Dissertation, 2022

Supervisor: Prof. Dr. Burç Mısırlıoğlu

Keywords: MoO_3, thin film, RF reactive sputtering, characterization

Molybdenum oxide thin films exhibit a variety of stable phases. They possess interesting structural, optical, chemical, and electrical characteristics that are appealing for a number of applications in energy storage, sensors, solar cells, infrared detectors, and smart windows. Additionally, molybdenum oxide thin films are mostly preferred in chemiresistive gas sensors, for sensitive detection of nitrogen dioxide (NO_2), carbon dioxide (CO_2), hydrogen (H_2), and ammonia (NH_3). In this study, optimized conditions of MoO_3 have been investigated for gas sensor applications. Molybdenum oxide thin films have been deposited by Radio Frequency (RF) magnetron sputtering on silicon wafers using a metallic molybdenum target in the presence of oxygen (O_2) and argon. In situ heat treatment was applied to form a better crystalline structure of molybdenum oxide thin films followed by an X-Ray Diffractometer (XRD), Scanning Electron

Microscopy (SEM), Photoluminescence, and Electron Paramagnetic Resonance (EPR) were used for the structural, stoichiometric, morphological, and defect concentration analyses respectively. The optical characteristics were analyzed by ellipsometry to gain insight into the semiconducting character of the samples and the sheet resistance was measured by the 4-Point Probe method. Considering the information gathered from the experiments, we discuss the growth conditions in the sputtering system and thickness effect to improve their structural qualities affecting their optical and electrical characteristics.

ÖZET

RF MAGNETRON SIÇRATMA TEKNİĞİYLE BÜYÜTÜLMÜŞ MoO$_3$ FİLMLERİN KARAKTERİZASYONU

Neslihan ŞİŞMAN

Malzeme Bilimi ve Nano Mühendislik, Yüksek Lisans Tezi, 2022

Tez Danışmanı: Prof. Dr. Burç Mısırlıoğlu

Anahtar Kelimeler: MoO$_3$, ince film, RF magnetron sıçratma, karakterizasyon

Molibden oksit ince filmler, çeşitli kararlı fazlar sergiler. Enerji depolama, sensörler, güneş pilleri, kızılötesi dedektörler ve akıllı pencerelerde bir dizi uygulama için çekici olan ilginç yapısal, optik, kimyasal ve elektriksel özelliklere sahiptirler. Ayrıca molibden oksit ince filmler, nitrojen dioksit (NO2), karbon dioksit (CO2), hidrojen (H2) ve amonyağın (NH3) hassas tespiti için kimyasal dirençli gaz sensörlerinde çoğunlukla tercih edilir. Bu çalışmada, gaz sensörü uygulamaları için optimize edilmiş MoO3 koşulları incelenmiştir. Molibden oksit ince filmler, oksijen (O2) ve argonun varlığında metalik bir molibden hedefi kullanılarak silikon gofretler üzerine Radyo Frekansı (RF) magnetron püskürtme ile biriktirilmiştir. Molibden oksit ince filmlerin kristal yapısını oluşturmak için yerinde ısıl işlem uygulandı, ardından yapısal ve stokiyometrik özellikleri için X-Işınları Difraksiyonu (XRD), morfolojik karakterizasyonu için

Taramalı Elektron Mikroskobu (SEM), Fotolüminesans ve Elektron Paramanyetik Rezonans (EPR) kullanıldı. Numunelerin yarı iletken karakteri hakkında fikir edinmek için optik özellikler elipsometri ile analiz edildi ve tabaka direnci 4 Noktalı Prob yöntemiyle ölçüldü. Deneylerden elde edilen bilgiler ışığında, optik ve elektriksel özelliklerini etkileyen yapısal niteliklerini iyileştirmek için püskürtme sistemindeki büyüme koşullarını tartışıyoruz ve kalınlık etkisini tartışıyoruz.

ACKNOWLEDGEMENTS

I would like to particularly thank my boyfriend Emre Baran for being here with unbelievable patience and love for me both in my undergraduate and graduate years. He made me get through when I was at the crossroad in my academic life. Thanks to him for being by my side and for the irrelevant (maybe one-day-relevant) accounting and management courses that we took together. Life would be so boring without you.

I owe deep thanks to my dear family, my mother Emine Şişman, my sister Reyhan Başaran, and my brother Ayhan Şişman. Especially, I would like to thank my father, Mehmet Şişman, who I always felt that he saw and protected me even though he was not by my side, and who contributed to my success in getting me to where I am today. I could have never achieved this without their strength and faith in me. They have supported me all the time I needed and always put my needs before theirs. I hope that I can be worth their efforts and good hearts.

To my beloved father Mehmet ŞİŞMAN…

TABLE OF CONTENT

LIST OF FIGURES

LIST OF TABLES

LIST OF EQUATIONS

LIST OF ABBREVIATIONS

Mo : Molybdenum

MoO_2 : Molybdenum Dioxide

β-MoO_2 : Monoclinic-Molybdenum Dioxide

MoO_3 : Molybdenum Trioxide

α-MoO_3 : Orthorhombic-Molybdenum Trioxide

β-MoO_3 : Monoclinic-Molybdenum Trioxide

h-MoO_3 : Hexagonal-Molybdenum Trioxide

γ-Mo_4O_{11} : Orthorhombic-Tetramolybdenum Undecaoxide

XRD : X-Ray Diffraction

SEM : Scanning Electron Microscopy

SE : Spectroscopic Ellipsometry

n : Refractive Index

k : Extinction Coefficient

RF : Radio Frequency

TMO : Transition Metal Oxide

Ar : Argon

O_2 : Oxygen

NH_3 : Ammonia

NO : Nitrogen Oxide

NO_2 : Nitrogen Dioxide

WO_3 : Tungsten Trioxide

V_2O_5 : Vanadium Pentoxide

Au : Gold

Pd : Palladium

PVD : Physical Vapor Deposition

EPR : Electron Paramagnetic Resonance

PL : Photoluminescence

cSi : Crystalline Silicon

Zn : Zinc

1. INTRODUCTION

The fields of synthesis have expanded as it can accurately control the size of both organic and inorganic materials [1] – [3]. Various developments in synthesis techniques have provided access to the tailoring of functional metal-based oxides for a variety of applications requiring specific functionalities [1]. In parallel, downscaling of device dimensions has turned attention to nanostructures: They have become one of the fundamental components of nanotechnology due to their high surface area to volume ratio, as well as the quantum size effects [4]. On the other hand, nanomaterials have become a common platform for the direct electrical detection of biological and chemical species with improved sensing capabilities among the numerous applications being studied [5] – [8]. Increased functionality and applicability in daily life are further goals of these investigations by focusing on one of the areas which are high-protein products such as meat can degrade quickly and affect human health due to widespread consumption, it has become necessary to control and monitor these high-protein content foods [9] – [12]. It is important to monitor and control food waste because the spoilage of food products, especially meat products, not only creates a problem for the health of the public but also creates a financial problem. According to the Food and Agriculture Organization of the United Nations [11], people waste about a third of their food, the financial cost of which amounts to 1 trillion dollars each year. Along with a high amount of meat waste, which causes both financial and physical damage to people, as well as determine that more than 20% of the carbon footprint of global food waste is the waste of spoiled meat. [11].

Based on the problems occurring with the issue of meat waste bring gas sensor arrays for the monitoring of meat spoilage solutions have gained a lot of attention [13], [14]. Gas detection technologies are effective in monitoring toxic gases emitted during meat spoilage, as well as gases that affect daily life [15], [16]. Among the gas sensor designs that have been developed and improved over time, resistivity-based sensors stand out with their lower cost and size [17]. For the detection of gases based on resistivity measurement during meat spoilage, metal oxides and mostly transition metal oxides are widely utilized with their high sensitivity, quick response, and low cost and power consumption.

For the resistivity-based sensor design, generally transition metal oxides (TMOs) are utilized which are countable as one of the most interesting classes among solids with their unique properties, structures, and applications [18], [19]. To emphasize the most significant properties of TMOs can vary in their outer d-electrons and possess unique and useful electronic, optical, and magnetic properties. These properties are dependent on the defects inside the material such as vacancies, dislocations, and grain boundaries [18] that determine in which application areas it might be used. One of the well-known uses for TMOs among the numerous applications that consist of the properties mentioned before is gas sensors. In gas sensor applications where TMOs are used, gas-sensitive oxide layers consist of materials such as molybdenum trioxide (MoO_3) [20], tungsten trioxide (WO3) [21], vanadium pentoxide (V2O5)[22], and so on. Most known and utilized MoO_3 [20], WO_3[21], and V_2O_5[22] thin films in gas sensor applications are produced for the detection of toxic and non-toxic gases and these thin films are produced by many techniques such as sol-gel, ion beam deposition[23], sputtering deposition [20], thermal evaporation [24], and spray pyrolysis [25]. In this study, MoO_3 has been chosen to investigate the role of defects in the structural, optical, and electrical properties of the sensing layer and the thin films have been deposited by radio frequency (RF) reactive sputtering [18] – [20].

1.1. MoO$_3$ as a Ceramic Material

To provide general information, molybdenum trioxide has interesting optical, structural, and electrical properties as a transition metal oxide semiconductor material which has applications in various areas being perovskite solar panels [26], crystalline silicon (c-Si) [27], storage devices, li-ion batteries [28], and sensors [29], [30]. For instance, in heterojunctions of c-Si, it facilitates low-resistance hole transport from the absorber which is explicitly needed for reducing the resistance of the hole transport devices. [27]. In addition, it also improves the stabilization of organic light-emitting devices for wearable display technology. Moreover, it is widely used as a gas and chemical sensor which stands out for its sensory properties, as it catalyzes the oxidation of hydrocarbons and the dehydrogenation of alcohols [30] since some molybdenum oxide compounds specifically MoO$_3$ are known to be cathodic electrochromic [31].

1.1.1. Structure

Molybdenum oxide can be found in many different stoichiometries and crystalline phases such as MoO$_3$, MoO$_2$, Mo$_8$O$_{23}$, Mo$_9$O$_{26}$, Mo$_4$O$_{11}$, and MoO$_2$ based on the oxidation state of Mo. It is known that the most stable phase the orthorhombic-MoO$_3$ (α-MoO$_3$) [32] and the metastable monoclinic-MoO$_3$ (β-MoO$_3$)[33] thermodynamically crystal phases are the two main crystal phases of MoO$_x$ [34], [20]. Based on this information, MoO$_3$ exists in the highly desired layered crystal phase known as orthorhombic-MoO$_3$ has a distorted MoO$_6$ octahedra that are arranged in dual-layer planar crystals and van der Waals forces hold these distorted MoO$_6$ octahedra together along the b axis [010] direction[35], [36]. Other covalent and ionic bonds make up the majority of the octahedra's internal bonds [34], [37].
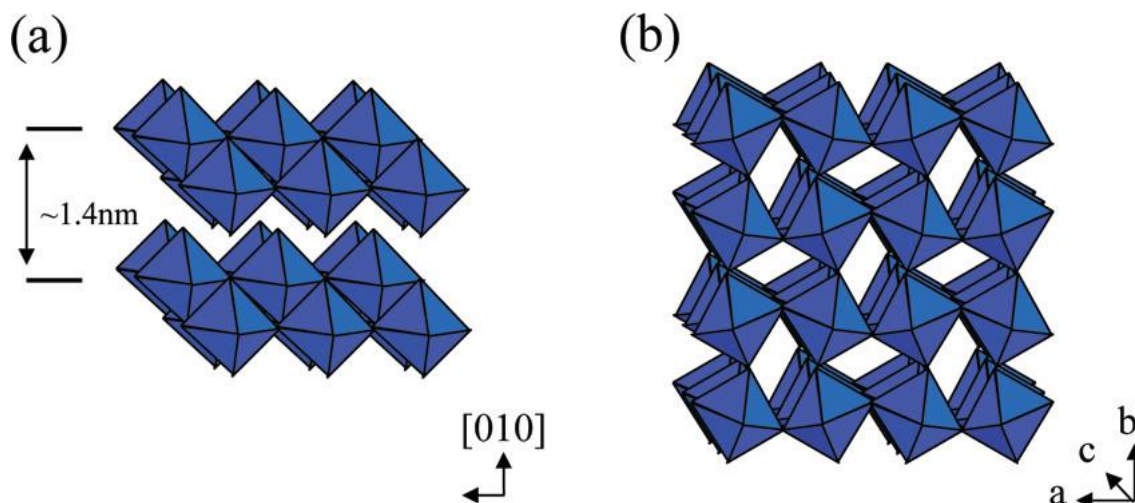
Figure 1. (a) Stable orthorhombic MoO_3 (b) metastable monoclinic-MoO_2 (Reprinted from Ref. [37], with the permission of ACS Publication).

The arrangement of the crystal structure is significant to understand the compounds of molybdenum oxide. As mentioned in the previous paragraph, α-MoO_3 which is the most stable one, has very unique layered structure and Figure 1 shows the layers are formed by atomically thin layers ~0.7 nm thick and then deposited to form secondary layers in bilayers of distorted Mo-O octahedra [34]. After each molybdenum bonded with oxygen, MoO_6 octahedra form rows of corner-sharing along the a-axis [100] plane and zigzag rows of edge-sharing along the c-axis [001] plane in each double layer. The internal connections between the atoms in double layers are mostly covalent and ionic which are strong bonds, whereas weak van der Waals forces are used to link the adjacent layers along the b-plane to produce a lamellar structure [37], [35].

1.1.2. Optical and Electrical Properties

Since MoO_3 is a transition metal oxide with high stability, n-type semi-conductivity, and nontoxicity that has received a lot of interest [38]. The optical and electrical properties of it requires a lot of attention to be used in the necessary field. Therefore, [39] the change in optical and electrical properties will have an effect on stoichiometry and crystal structure, and it is important to understand the relation between them [39].

These different stoichiometries and phases allow researchers to engineer the band gap of thin film materials from the wide band gap to lower. For instance, the band gap of MoO_3 is 2.39-3.40 eV [22], [40] to the more conducting one MoO_{3-x} and then the semi-metallic MoO_2 has 1.83 eV [41] and eventually to the metallic, thin film in the form of metallic Mo. When x is in the range between 2 and 3 which contains a mix of different molybdenum oxide compounds, the values of the band gaps have been as 2.4 to 2.7 eV [42]. Generally, the sub-stoichiometric MoO_3 with mid-gap states made use of the majority of the reported devices [40], [43] – [45]. Based on a band transition energy which is approximately 4.15 eV corresponds to the Mo^{5+} $d_{xy} - d_{yz}$ band transition of a severely distorted polyhedron according to the crystal field model [46]. The smaller dimension of these nano-structured materials may be the cause of the increased band energy compared to the previously reported value (3.88 eV). Strong electron-lattice coupling interaction is demonstrated by the relatively huge gap between the two bands. Moreover, the relation between the thickness and the band gap for MoO_3 thin film shows there is an inverse proportion which indicates that the increase in thickness outcome with the decrease in the band gap. According to the reports, the reason for this is attributed to the change in barrier height caused by the grain size in polycrystalline films and high-density dislocations or quantum size effect [47]. Slater states [48] that barrier height can vary due to the charge accumulation at the grain boundaries and the energy barriers are linked with this charge accumulation [49].

The electronic structure of MoO_3 is in good harmony with Scanlon's modeled X-ray photoemission spectra [49]. It has been stated that the effects of the localization of electrons on the surface vacancies on the electronic properties were examined by other studies [50], [51]. According to Scanlon's model, 4d states of Mo are filled with electrons donated from the oxygen vacancies, which then exist as gap states in the band gap [51], [52]. These 4d states of Mo are filled during the formation of Mo-Mo bonds is responsible for shear structure's stabilization of oxygen-deficient MoO_3 [51], [53]. For this reason, oxygen vacancies offer n-type doping that through band bending and charges transfer doping, permits the alignment of band levels with metals, oxides, and organic molecules that enables to be used of MoO_3 in a hole conductor in organic electrical devices due to its high work function [52], [54]. Furthermore, despite the fact that MoO_3 has a high band gap for the device applications, the band gap is reduced by electron doping providing the lattice distortion of MoO_3 in order to be utilized

efficiently as a hole conductor in solar-energy applications [54],[55],[56]. Over and above that, because of Fermi level states caused by Mo^{4+} ions. [57], amorphous non-identified, MoO_x, films have demonstrated a metallic band structure. Even though the lattice structure of MoO_x was not identified, a transition to correlated metal conduction was shown to occur near x = 2.6 [58].

1.2. Thin Film Deposition

There are many deposition methods reported in the studies for thin films such as sputtering [63] – [65], molecular beam epitaxy [62], [63], spray pyrolysis [64], [65], sol-gel, chemical bath deposition [66], [67], thermal evaporation [68], [69], pulsed laser deposition [70], and dip coating [71]. In this study, the deposition method performed for MoO_3 is radio frequency (RF) reactive sputtering. To understand the properties of the material, it is crucial to know the deposition technique that is used. Hence, the sputtering method will be explained in detail in the next section.

1.2.1. Radio Frequency Magnetron Sputtering

Over the past ten years, magnetron sputtering has advanced quickly to the point where it is now recognized as the preferred method for depositing a variety of crucial industrial coatings. This expansion has been propelled by the rising need for high-quality functions in numerous diversified market sectors. Magnetron-sputtered materials can now perform as well as thicker materials created by other physical vapor deposition (PVD) technologies and can often give the same functionality [72]. The physics underlies the concept of sputtering is to understand the mechanism of the process that sputtering is one of the deposition types of non-equilibrium processes at the energy range of interest and it takes place when an energetic particle hits the surface of the solid target. This energetic particle can be an ionized gas or a photon that has sufficient energy to eject the atom from the surface of the target [73]. This phenomenon is called glow discharge. The ion bombardment resulting in the glow discharge also causes secondary electrons to be released from the target surface, and these electrons

6

are crucial for maintaining the plasma [74], [75]. Yet, there are limitations to the sputtering deposition such as low ionization efficiency in the plasma, low deposition rates depending on the plasma quality, and substantial heating effects. Over the years, these limitations have been overcome with unbalanced magnetron sputtering [72].

One of the significant parameters in sputtering technique due to provide controllability is the deposition rate which is the rate of the thickness of the film formed by the atom reached out to the substrate from the target surface per minute. Generally, the deposition rate is changing between 50 and 500 Å/min [76]. However, some problems may occur during the deposition. For instance, the ion ejected from the target surface may be reflected, the ion can be trapped inside of the target, or radiation damage can occur which means that lattice defects can be created with the incoming ion. Correspondingly, sputtering occurs as a result of the separation of the atom from the solid target as a result of ion bombardment by momentum transfer without the mentioned problems [76].
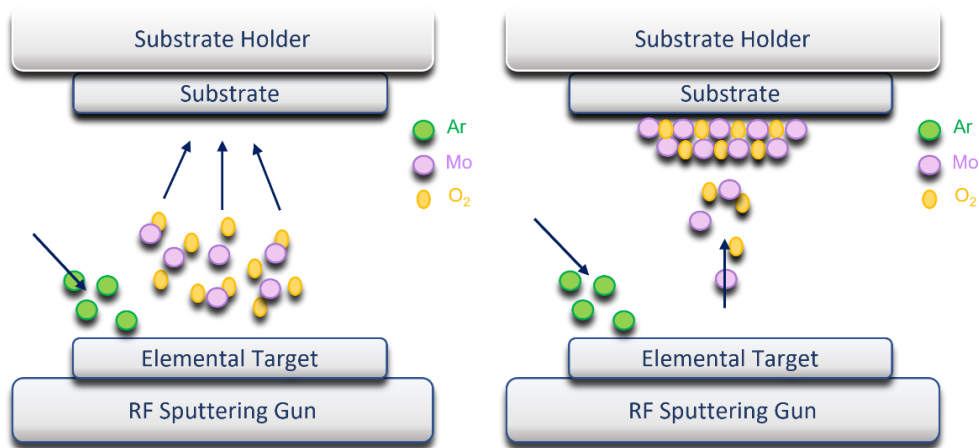
Figure 2. Scheme of sputtering growth technique.

Figure 2. Scheme of sputtering growth technique. that helps to visualize the concept of how the atoms are sputtered and forming a film. The substrates and the targets are placed into a closed chamber kept under a high vacuum in order to avoid contamination during the deposition and increase the film quality. A low-pressure inert gas, which is generally argon introduced to the chamber, and high voltage is applied between the

substrate and the target. High voltage provides a medium that helps to ionize and energize the inert gas to create plasma. Atoms that have high enough energy to reach the substrate and low enough to form the desired structure form the thin film to reach desirable amount of deposition rate with high quality film. As the problems during the deposition mentioned previous paragraph, reflected ions can accumulate on the target surface and radio frequency is used to prevent charge accumulation on the target surface [81] – [83].
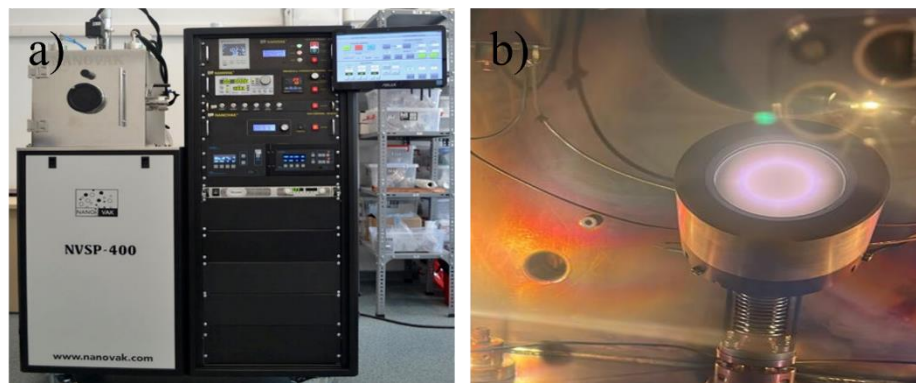
Figure 3. a) NANOVAK-400 sputtering device used in this work b) Plasma formation during the deposition.

Average RF and DC ion currents are not different that much. With a voltage of 1000V applied and a current density of 1 mA/cm^2, t would be equivalent to 1 µs for a quartz substrate with a typical capacitance of 1 pF/cm^2. Therefore, for frequencies exceeding 1 MHz, a continuous discharge can be sustained [76] resulting in the generation of RF plasma by electron ionization. The electron ionization is conducted by the RF magnetron frequency which oscillates at 13.56 MHz and exceeds 1 MHz for the continuous discharge. However, the mechanical inertia of the ions prevents them from continuing these oscillations at the frequency. The voltage of the RF discharge decreases resulting from this excitation, which is far more efficient than ionization by secondary electrons which are not oscillating. Therefore, the target behaves more like an anode than a cathode during the positive half-cycle. For this reason, the surroundings of the substrate have much more plasma density for RF [80] which means there is less need for a gas medium scattering of the sputtered target atoms [76]. The possible scenario varies from the gas medium scattering is that the arc generation brought on by

dirt particles on the target surface is another issue with glow discharges. Due to the rapidly alternating field in RF systems, maintaining the arc is more challenging [76].

1.2.1.1. Reactive Sputtering

Compound films are deposited by both the compound target and the elemental target. When the elemental target is used to deposit compound film, the reactive gas is introduced to the system besides the inert gas. These reactive gases can be O_2, N_2, and CH_4. This process is called the reactive process or reactive sputtering generally when chemical binding occurs between two or more chemical elements at least one of them is metal and the other one is not [81]. By adding a suitable reactive gas to the noble sputtering gas, reactive sputtering can produce a variety of compounds from a cheap metal target. Compounds represent the substantial commercial value among the majority of thin films and coatings which makes reactive sputter deposition a topic of significant industrial and technological interest [82]. Generally, oxides and nitrides [83] compounds are preferred to deposit to satisfy the industrial interests and demands besides borides [84], carbides [85], sulfides [86], and selenides [87].

Since the energy and momentum cannot be conserved in a two-body collision, the reaction between the reactive gas and the sputtered species cannot take place in the gas phase at the normal sputtering gas pressured which is lower than 2 Pa used in reactive sputter deposition [81]. Reaction doesn't take place only at the substrate or chamber walls but on the cathode target surface as well, because the target surface acts as a third body for the reaction [88], [89]. Material affects the sputter yield and secondary electron emission. Therefore, the total sputter process can be influenced by the reaction at the target surface. The yield of the elemental target is much higher than the yield of the compound target material, resulting in an increase in the flow rate of the reactive gas with a drop in the deposition rate. Because fewer reactive gas species are consumed and fewer atoms of the elemental target material are sputtered, the reactive gas partial pressure suddenly and sharply increases, and the resulting deposited layer becomes rich in reactive gas species. As a result, there is a non-linear relationship between the compound film composition and the rate of reactive gas flow similar to how the flow

rate of the reactive gas affects the deposition rate and the relation between them is not linear [88].

1.2.2. Effect of Deposition Parameters on Thin Film Growth

There are some parameters that can affect the thin film properties and its growth conditions:

- Substrate temperature,
- Base pressure,
- Sputtering gas pressure,
- Reactive gas pressure,
- RF power,

The first parameter is the substrate temperature affects the mobility of adatoms. Thus, an increase in the substrate temperature induces adatom mobility and enhances structural homogeneity. The substrate temperature is generally optimized according to the best texture. For instance, above 400°C is not preferable due to microcrack formation [90]. Afterwards, base pressure determines the number of particles inside the chamber. If the number of particles is high, the number of collisions will be high as well which affects the number of particles adsorbed by the substrate negatively. In addition, an increase in the pressure inside the chamber reduces the deposition rate and the film stoichiometry. The other parameter which is the total sputtering gas pressure has a crucial role during the reactive sputtering process. Besides Ar the introduced gas to the chamber determines the formation of the compound. Some metals tend to grow oxygen depleted such as Zn and Mo result in the oxygen vacancies and interstitials tend to form during the deposition [91]. For this reason, the oxygen partial pressure amount that is given to the chamber can be increased after a while in order to maintain the stoichiometry. The final parameter, RF power has a positive impact on the adatom energy and microstructure formation. Since the adatom mobility increase, the energy of the incident particle increased on the substrate surface. Thus, the crystallinity of the film is enhanced with the denser and better-oriented film. On the other hand, RF power

can cause a negative effect on the sputtering yield and the deposition rate. The adatoms should have enough energy to reach the substrate, whereas when the adatoms' energy is too high, the number of collisions increases, and the possibility of reaching the substrate reduces [89].

1.2.3. Structure Zone Model

The relation between the deposition parameters and the film produced by sputtering has been mentioned in the previous section. By giving detailed information about the microstructure of the thin film formed by the sputtered atoms called adatom which lies on the crystal structure based on the structure zone model will be elucidated in this section. The quantity of energy and the mobility of the adatoms on the surface affect the microstructure of thin films. The substrate temperature and incident ion energy, which are principally controlled by the chamber pressure and the intense particle bombardment of the film during deposition, are responsible for determining the energy and mobility of the adatom [92] The adatom movement is rather modest during this process and there is a one-sticking coefficient which is the shadowing effect. Shadowing produced a film with a network of interconnected voids that delineated columns of material and a low number of nuclei due to the low adatom mobility, columns also developed in a power-law shape, generating hierarchical aggregates and cauliflower-like structures, which are collections of more compact and equiaxed grains [93], [94].
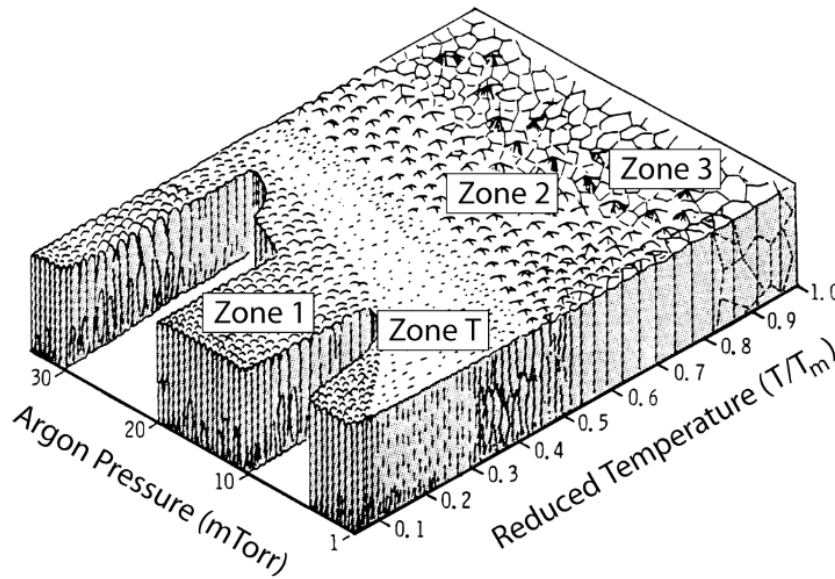
Figure 4. Structure Zone Model developed by Messier and Trolier-McKinstry [95] .

In Figure 4, the structure zone model has been demonstrated and will be explained in further. As seen in figure, Zone T represents the transitional area consisting of Zone 1 and Zone 2 consist of strong grain boundaries and tightly packed, fibrous grains were the results of the elevated substrate temperature dependent on the rising gas pressure result in the temperature for the transition zone shifted to higher temperatures. Zone 2 is explained by the surface diffusion increased with the homologous temperature (T_h) due to the enhanced adatom mobility brought on by T_h. With the increased width, increased density, and clearly defined grain boundaries, surface diffusion becomes higher [94]. The activation energy for metallic films was of the same order of magnitude as that for surface diffusion and was also comparable to that for diffusion along grain boundaries, and as the temperature increased, the Zone 2 columns are getting complicated. Zone M is dependent on Zone T in terms of pressure in which with the easing pressure, matchstick morphology starts to occur, and the columns are parallel to each other in this zone. In Zone 3, a highly dense structure with equiaxed grains starts to form with increased T_h. The nucleation and growth processes are in competition when the first few monolayers are forming. The proportions of the island and the layers are determined by their respective weight. An island-type of growth is noticed when the bonding between the atoms or molecules of the film material is greater than the bonding between the film and substrate [93], [96].

2. EXPERIMENTAL PROCEDURE

2.1. Substrate Preparation
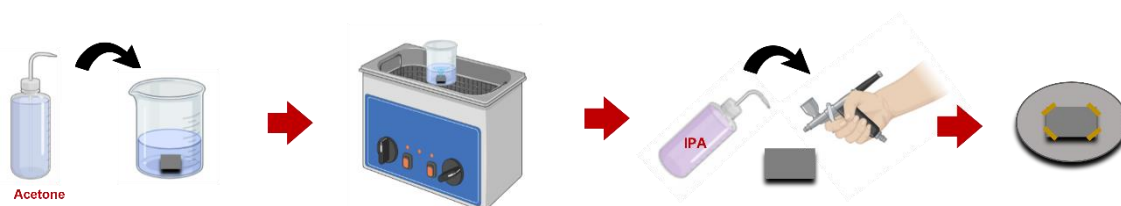
Figure 5. Scheme of the substrate preparation before the deposition.

Substrates should be selected and prepared carefully to determine the final thin film properties properly. Since different substrates have different structures and mechanical and optical properties, three types of substrates were used which are, [001] Si wafer, MgO (magnesium oxide), and Al_2O_3 (sapphire). The dimensions of Si wafer and Al_2O_3 substrates are given respectively as 1x1 cm^2 and 1.5x1.5 cm^2 sizes. In Figure 5their cleaning process was demonstrated which consists of acetone and alcohol cleaning. Substrates were cleaned under ultrasonic vibration with acetone for 10 min at room temperature. Then, they were cleaned with isopropanol and dried under a nitrogen jet. Teflon tweezers were used during the cleaning process to avoid scratches on the substrate. After the cleaning process, substrates were put on the substrate holder by using tape placed into the chamber for the deposition.

2.2. Film Deposition

Molybdenum oxide thin films were deposited with the reactive sputtering method at NANOVAK-400 device which is in Sabancı University Nanotechnology Research and Application Center (İstanbul, Turkey). Pure (99.95%) metallic molybdenum target (Adesis) was used as a cathode and O_2 partial pressure gas was given into the chamber for the reactive sputtering. The diameter of the target is 50 mm, and the target-to-substrate distance is 120 mm. Before the deposition, residues in the chamber from previous depositions were cleaned with ethanol and a vacuum cleaner. In addition, the shutter in front of the substrate holder, the housing ring of the target, and the substrate holder plate were also cleaned with ethanol.

The chamber was put under vacuum to approximately $2x10^{-6}$ mTorr. Afterward, Ar gas was introduced to the chamber and generated the plasma in order to clean the contamination on the target surface during the pre-sputtering process. At the end of the pre-sputtering process, O_2 gas is sent through the chamber to form a molybdenum oxide compound, especially for tuning the MoO_3 compound. For tuning the MoO_3, the deposition parameters such as power, sputtering pressure, partial pressures of Ar and O_2 gases, and substrate temperature optimization were one of the aims of this study.

Table 1. Optimization of Ar and O_2 partial pressures.

Target	Power (W)	Working Pressure (mTorr)	Time (min)	Partial Pressure Gas of Ar (%)	Partial Pressure Gas of O_2 (%)	Substrate	Temperature (°C)
Mo	150	15	40	100	0	Si	RT
Mo	150	15	40	80	20	Si	RT
Mo	150	15	40	60	40	Si	RT
Mo	150	15	40	40	60	Si	RT
Mo	150	15	40	20	80	Si	RT

Molybdenum oxide thin films were deposited on [001] Si substrate at room temperature under different partial pressures of Ar and O_2 shows the power and sputtering pressure

were kept at the same value and the variable parameter was partial pressures of Ar and O_2 gases. Molybdenum oxide thin films were grown in a mixture of (Ar+O_2) gasses being introduced into the chamber through mass flow controllers in order to get a total working pressure of 15 mTorr. The RF power was 150 W is enough to keep the deposition rate at moderate level.

2.3. Post Heat Treatment
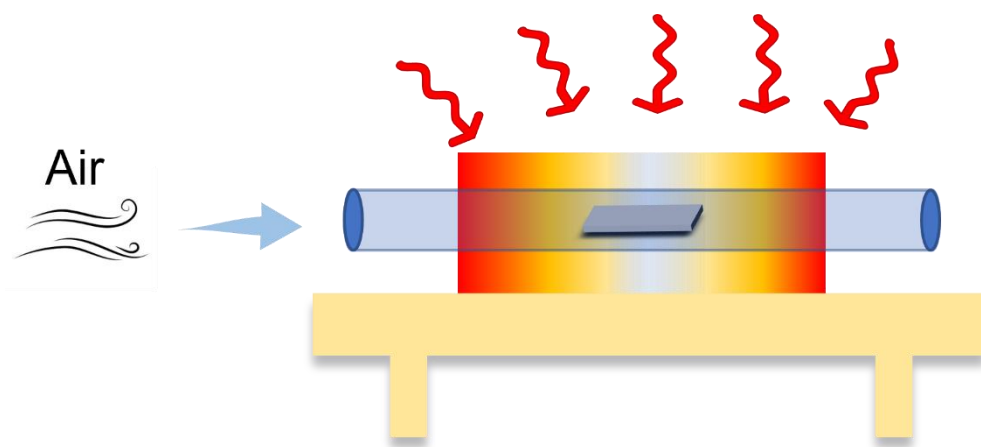
Figure 6. Post-heat treatment of metallic molybdenum after the deposition under air atmosphere.

The metallic Mo thin film was deposited by RF magnetron sputtering in the presence of 100% Ar on a silicon wafer at room temperature. The metallic Mo thin films were annealed in the air atmosphere at the furnace at different time durations. The aim was to oxidize the Mo atom with oxygen existing in the air. However, the air is made up of approximately 78% of nitrogen, 21% of oxygen, and small amounts of other gases [97] which means air is not the pure oxygen source for the annealing.

Table 2. Post-Annealing Parameters.

Target	Power (W)	Working Pressure (mTorr)	Time (min)	Partial Pressure Gas of Ar (%)	Temperature During Deposition (°C)	Post Annealing Temperature (°C)	Annealing Time (min)	Substrate
Mo	150	15	30	100	RT	500	0	Si
Mo	150	15	30	100	RT	500	15	Si
Mo	150	15	30	100	RT	500	30	Si
Mo	150	15	30	100	RT	500	45	Si
Mo	150	15	30	100	RT	500	60	Si
Mo	150	15	30	100	RT	500	120	Si

In Table 2, post-annealing parameters were given with the deposition conditions. On top of Si substrates, metallic Mo was deposited for 30 minutes at room temperature and put inside the furnace under the air atmosphere. All molybdenum thin films were annealed at 500°C for different time durations. First, extreme annealing times were attempted to see the effect on the structure. Since the desired phase could not be obtained, the time intervals between the extreme ones were performed.

2.4. In-situ Deposition Treatment

Heater
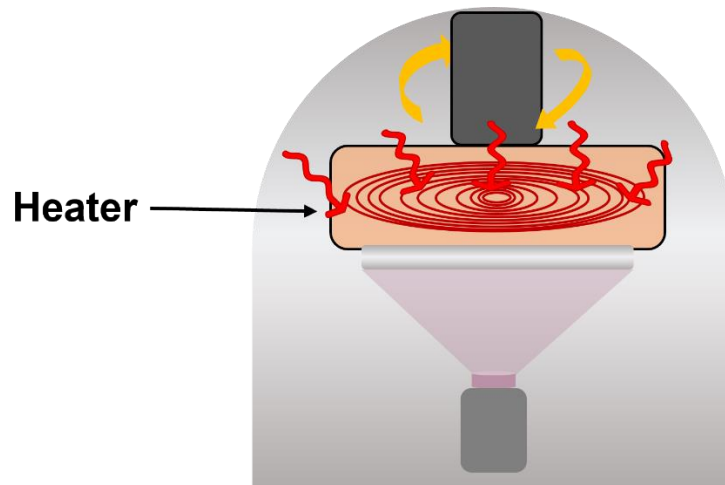
Figure 7. In-situ heat treatment during the deposition under the oxygen partial pressure atmosphere.

Table 3. Optimization of in-situ heat treatment temperature.

Target	Power (W)	Working Pressure (mTorr)	Time (min)	Partial Pressure Gas of Ar (%)	Partial Pressure Gas of O_2 (%)	Substrate	Temperature During Deposition (°C)
Mo	150	15	10	60	40	Si	350
Mo	150	15	10	60	40	Si	400
Mo	150	15	10	60	40	Si	450

Table 3 shows different temperatures were applied during deposition to get the best crystalline structure of MoO_3. The only variable parameter was the in-situ temperature such as 350, 400, and 450°C, and the temperature was applied to just the sample holder where the samples were placed. Power and working pressure were kept the same. According to XRD analysis of in-situ deposited samples, 400°C was chosen as the deposition temperature with the highest intensity given of MoO_3.

Table 4. Thickness optimization of molybdenum oxide thin films on Si wafer.

Target	Power (W)	Working Pressure (mTorr)	Time (min)	Partial Pressure of Ar (%)	Partial Pressure of O_2 (%)	Substrate	Temperature During Deposition (°C)
Mo	150	15	10	60	40	Si	400
Mo	150	15	20	60	40	Si	400
Mo	150	15	30	60	40	Si	400
Mo	150	15	40	60	40	Si	400

In Table 4, after setting all the parameters that can vary the phase and structure of the MoO_3. The thickness increased by the deposition time increase in order to see the thickness effect on the microstructure, and optical and electrical properties of the thin film by keeping all other parameters the same.

Table 5. Thickness optimization of molybdenum oxide thin films on Si, MgO, and Al$_2$O$_3$ substrates.

Target	Power (W)	Working Pressure (mTorr)	Time (min)	Partial Pressure of Ar (%)	Partial Pressure of O$_2$ (%)	Substrate	Temperature During Deposition (°C)
Mo	150	15	10	60	40	Si	400
Mo	150	15	20	60	40	Si	400
Mo	150	15	30	60	40	Si	400
Mo	150	15	40	60	40	Si	400
Mo	150	15	10	60	40	MgO	400
Mo	150	15	20	60	40	MgO	400
Mo	150	15	30	60	40	MgO	400
Mo	150	15	40	60	40	MgO	400
Mo	150	15	10	60	40	Al$_2$O$_3$	400
Mo	150	15	20	60	40	Al$_2$O$_3$	400
Mo	150	15	30	60	40	Al$_2$O$_3$	400
Mo	150	15	40	60	40	Al$_2$O$_3$	400

Table 5 shows the parameters of the deposition of molybdenum oxide by reactive magnetron sputtering. By using the metallic molybdenum in the presence of Argon and oxygen (O$_2$) gas, molybdenum oxide was deposited on various substrates such as silicon wafers, glass, and magnesium oxide (MgO), sapphire (Al$_2$O$_3$). On all substrates, the same power, working pressure, partial pressure of Ar and O$_2$ gases, and temperature were applied in order to compare the substrate effect on the structural and morphological properties of molybdenum oxide thin films. The variable parameter was deposition time and according to the increase in time, the thickness of the thin film also increased.

The first characterization tool was XRD to analyze the structure of the thin film. After getting the crystalline peak of molybdenum oxide, other analyses have been done before applying heat treatment to the films. The purpose of the heat treatment was to analyze the effect of heat treatment on the crystalline structure and the phases in

structure, reflectance and absorbance in optical properties, sheet resistance in electrical properties, and morphology at the surface of the thin film.

2.5. Material Characterization

2.5.1. Crystal Structure by XRD

XRD measurements were carried out Bragg-Brentano configuration using a Bruker diffractometer with point focus geometry under Cu K_α wavelength (1.5418 Å) radiation and a 0D Lynxeye detector in order to confirm the structure of the thin films. All these deposited molybdenum oxide thin films were analyzed by XRD with a range of angle of X-Ray from 5 to 90°. Incident X-Ray scanned the surface of the film to analyze the structure, lattice parameters, and angle of incidences to see the directions of crystallinity.

2.5.2. Microstructure by SEM

Zeiss Gemini-SEM using a field emission gun was utilized to see the morphology of the thin film surface. 5.2 kV was applied as an extraction voltage. The electron high tension (EHT) value was 3 kV. Both top-view and cross-view images were magnified from 20000X to 150000X. In this way, continuous and homogeneous film formation on the substrates was determined. Before SEM analyses, samples were coated with gold (Au) / palladium (Pd) to increase the conductivity of the sample.

2.5.3. Optical Measurement and Band Gap Calculation by Ellipsometry

Absorbance graphs of the molybdenum oxide films were obtained by Woollam spectroscopic ellipsometry (SE) stands for determining the optical, physical, and topographical properties of the thin film. It is operated in the range of 1.25 to 4.97 eV

photon energy (250-1000nm). Spectroscopic ellipsometry measurements were carried out at 65°, 70°, and 75° angles of incidence, and the ellipsometric data were fitted using a single-layer model. The absorption coefficient was calculated by the extinction coefficient (k) value and the band gap was found by the Tauc plot.

2.5.4. Photoluminescence and Electron Paramagnetic Resonance Measurement for Defect Analysis

Measurements of photoluminescence (PL) were made using an Edinburgh Instrument Spectrofluorometer FS5. The samples were evaluated at room temperature using an excitation wavelength of 260 nm and an excitation and emission bandwidth of 8 nm. It is an important instrument for comprehending the crystalline quality and locating contaminants in the substance.

A Bruker EMX Nano spectrometer with 2 G modulation amplitude, 0.31 mW microwave power, 500 scans with a sweep duration of 200 s, and X-band (9.64 GHz) continuous-wave EPR measurements were performed at room temperature.

2.5.5. Sheet Resistance Measurement by 4-Point Probe

Van der Pauw's four-point probe method was performed for investigating the electrical properties such as electrical resistivity (ρ_e) and sheet resistance (R_s) of molybdenum oxide films at room temperature. A 4-Point Probe was utilized to draw the I-V curve. The distance between the current and voltage points was known as 1mm Again, the effect of the deposition parameters, in-situ, and post-heat treatments on the electrical properties of molybdenum oxide films was analyzed to determine the semiconductor characteristics of the material.

3. RESULTS AND DISCUSSION

Results of the experimental work on MoO_3 thin film production and characterization are presented in this chapter. The results are categorized under the subgroups which are the general crystal structure of the as-deposited MoO_3 thin films, effects of post and in-situ heat treatment on the thin film crystal structure and morphology, molybdenum oxide thin films on a different substrate, and effect of thickness on the composition.

3.1. General Structure of the As-deposited MoO₃ Thin Films at Different Partial Pressures of Sputtering Gas
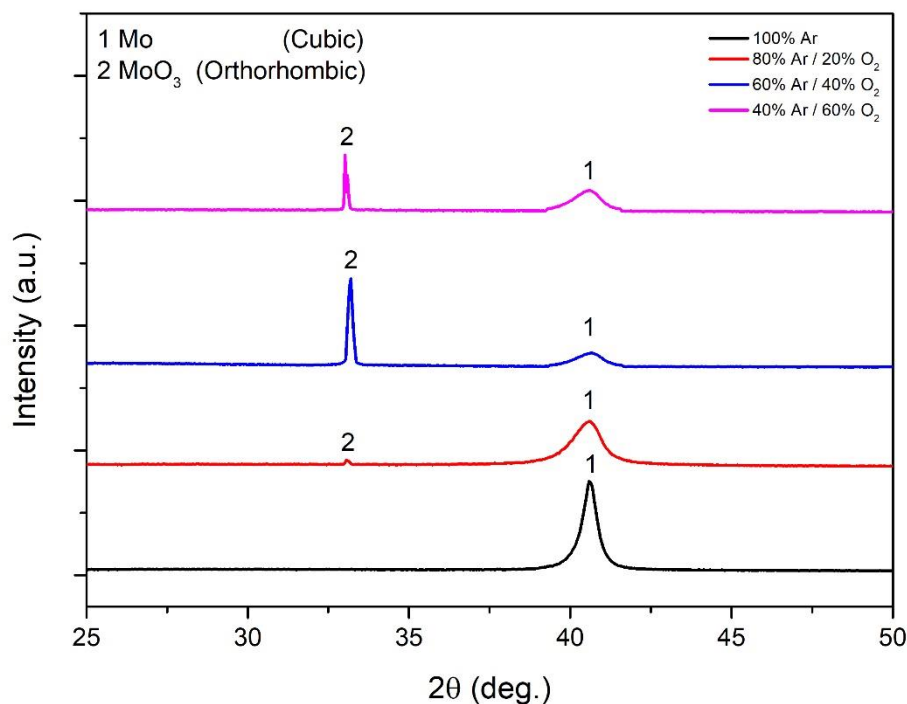
Figure 8. XRD graph of molybdenum oxide thin film at different partial pressures.

Figure 8, Molybdenum oxide thin films were deposited by reactive sputtering in the presence of different percentages of Ar and O_2 atmosphere at room temperature for 40 minutes by a metallic molybdenum target. XRD analyses show the existence of the crystalline structure of orthorhombic-molybdenum trioxide (α-MoO₃) on the substrate with a 2θ peak at 33.065° corresponding to (101) plane. However, the dominant phase of the thin film was metallic molybdenum with a 2θ peak at 40.5^0 in a cubic structure. In order to form molybdenum oxide compounds, heat treatment was applied during deposition to analyze the effect of in-situ and ex-situ heat treatment. According to the XRD spectra as a function of different partial pressures of argon and oxygen, 60% of Ar and 40% of O_2 atmospheric condition was chosen. After the in-situ heat treatment was applied, the metallic molybdenum peak disappeared and was converted into the α-MoO₃ while after the ex-situ heat treatment multiple phases start to evolve.

3.2. Post-Annealing on Thin Film Composition and Microstructure
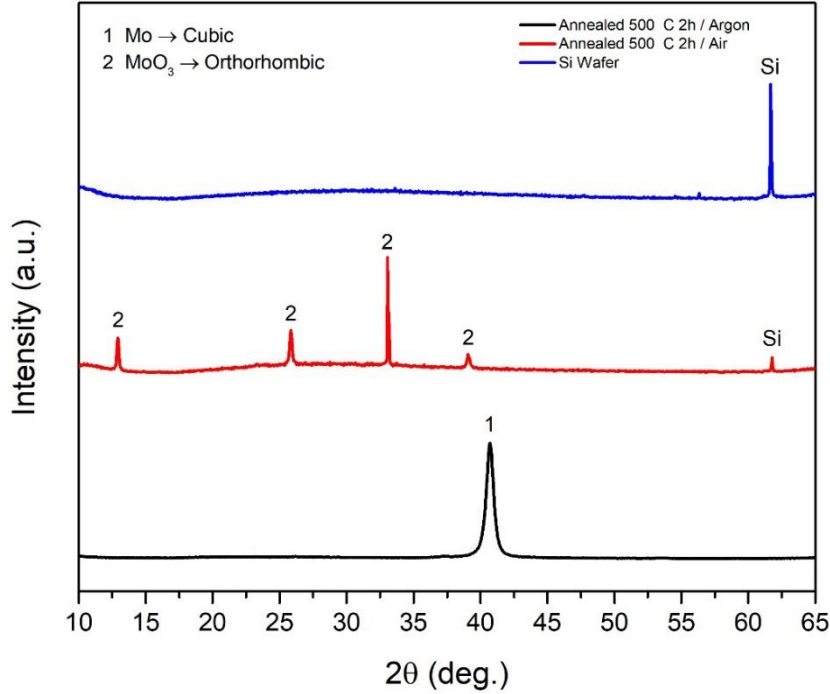
Figure 9. XRD graph of 2 hours post-annealed metallic molybdenum thin films in the presence of air.

In Figure 9, XRD analysis of the as-grown sample which was post-annealed at 500°C for 2 hours under both Ar and air atmosphere in the furnace was shown. The black line shows that the metallic molybdenum with a cubic structure still remained after post-annealing at a degree of 41°. However, when the as-grown sample was annealed at 500°C under air atmosphere for 2 hours, the phase was completely changed from metallic molybdenum to α-MoO_3 at 14°, 26°, and 33°. Hence, the formation of α-MoO_3 during post-annealing under air atmosphere was confirmed by the XRD spectrum.
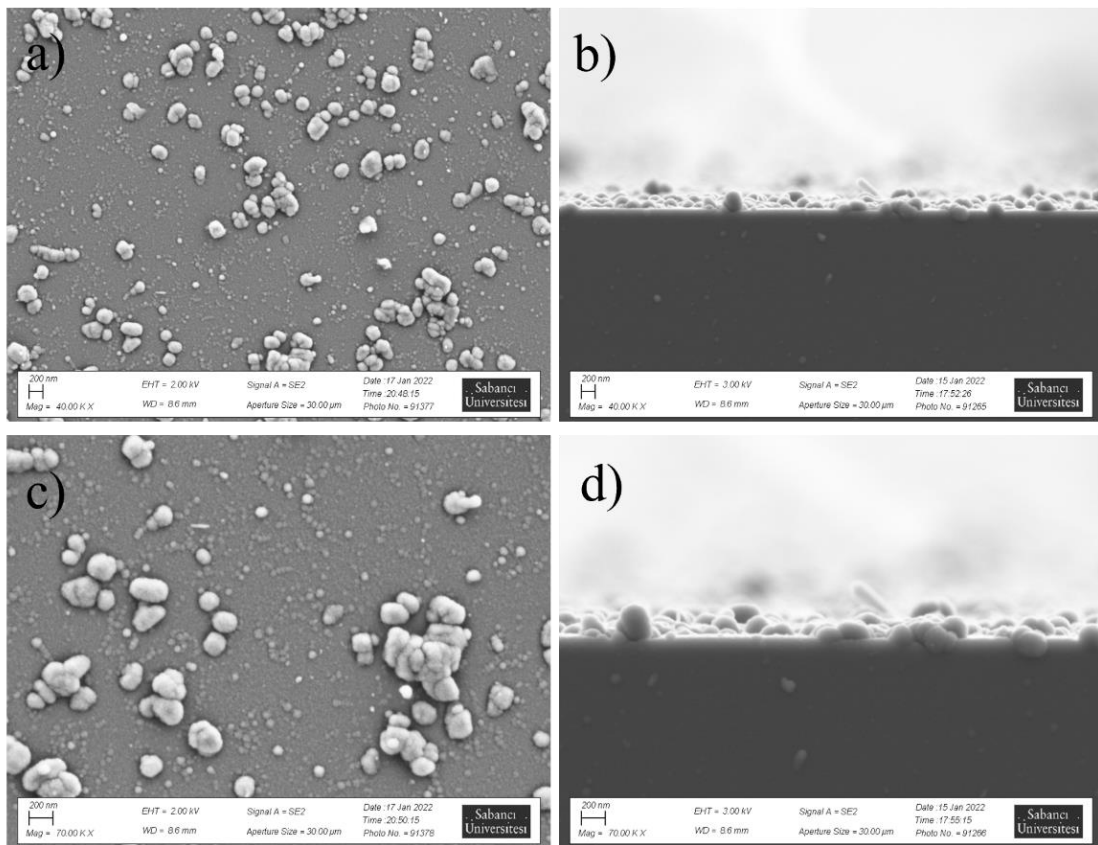
Figure 10. SEM images of 2 hours post annealed metallic molybdenum thin film in the presence of air a) Top-view 40000X b) Cross-view 40000X c) Top-view 70000X d) Cross-view 70000X magnifications.

In Figure 10, 2 hours annealed sample under air atmosphere was performed by SEM. According to the top-view images, big chunks of α-MoO₃ started to form instead of homogeneous and continuous film and they become islands. Hence, 2 hours of annealing under an air atmosphere is too long to protect the film's morphology. Additionally, big nanostructure affects the performance of molybdenum oxide thin films in sensing layer applications. The smooth and smaller size of the particles increases the surface area to volume ratio and it enhances the penetration of the target gasses as a gas sensing layer. Since 2 hours of post-annealing causes large nanostructures and removes the film homogeneity, the films were treated to heat for a shorter time.
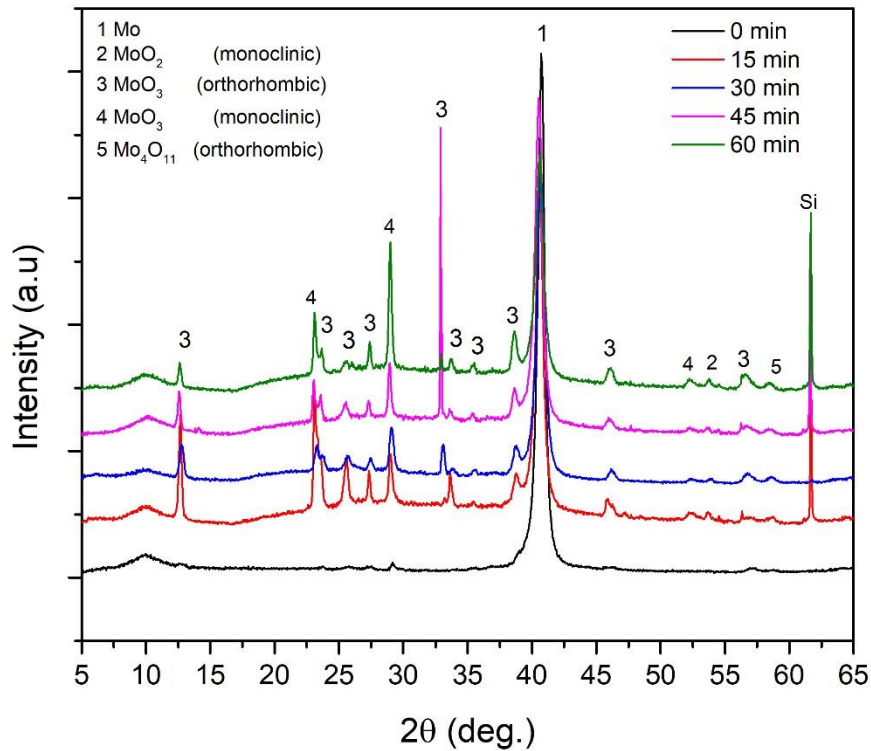
Figure 11. XRD graph of post-annealed metallic molybdenum thin films at different time durations.

As it seems in Figure 11, many phases other than MoO_3 were observed in the samples subjected to post-heat treatment for less than 2 hours. In addition, it was observed that the metallic molybdenum peak is still not completely converted to molybdenum oxide. In other words, while large islet structures were formed in the samples that were heat treated for a long time, the desired phase could not be tuned in the samples that were heat treated for less time. At the same time, since there was no mass flow controller, the amount of oxygen inside could not be adjusted, and for this reason, annealing was performed in the air. Thin films annealed in air, crystallized uncontrollably and the desired phase could not be reached. According to the side-view images, rough surface can be observed.
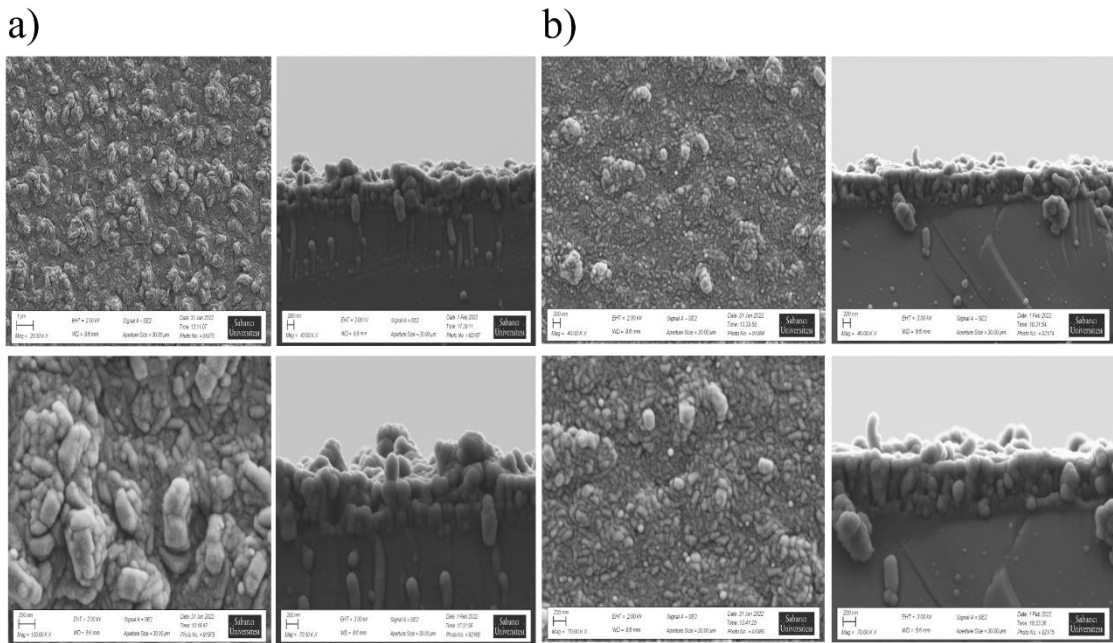
Figure 12. a) Top and cross-view SEM images at a magnification of 20000 and 100000X of 15 minutes post-annealed metallic molybdenum thin films in the presence of air atmosphere b) Top and cross-view SEM images at a magnification of 20000 and 100000X of 60 minutes post-annealed metallic molybdenum thin films in the presence of air atmosphere.

Since, 2 hours of post-annealing of metallic molybdenum thin film under air atmosphere causes island formation and deform the film homogeneity as shown in Figure 10, post-annealing was carried out at intervals of 0 and 60 minutes. Figure 12 shows that homogeneity and smoothness disappear, and forms large, disorganized structures. The surface of the film was very rough, yet 60 minutes air-annealing was not enough to form molybdenum oxide compound entirely.

3.3. In-situ Heat Treatment on Thin Film Composition and Microstructure
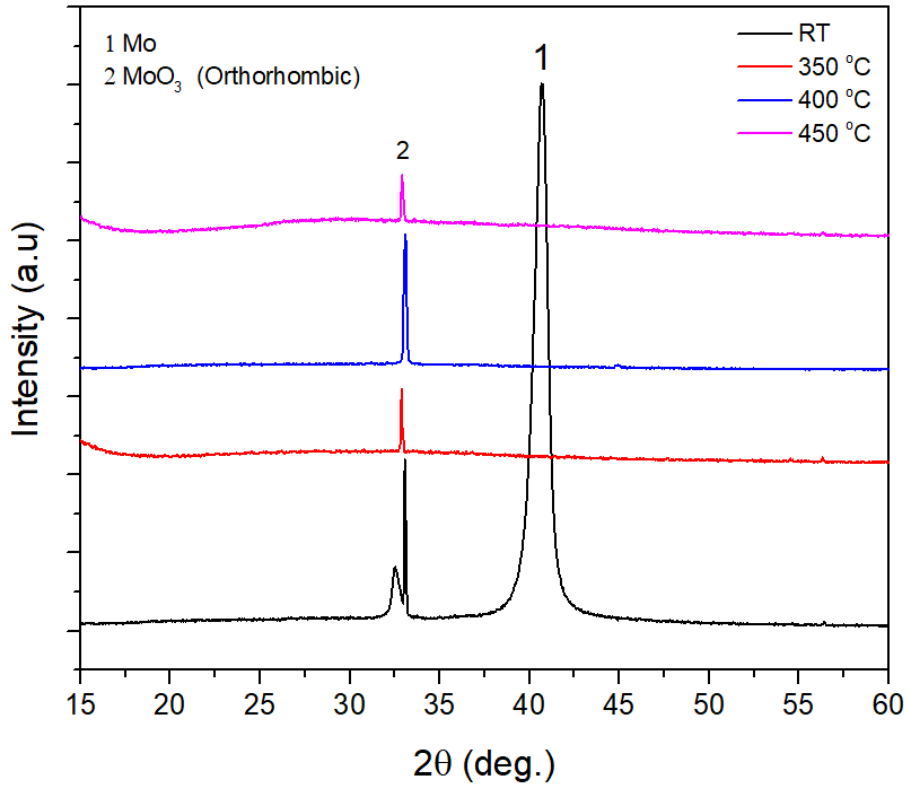
Figure 13. XRD spectra of reactively sputtered molybdenum oxide thin films with different in-situ heat treatment temperatures.

In Figure 13, it was produced by using a Mo target with an RF magnet sputtering method by giving temperature during deposition. XRD graphs of metallic Mo films produced at different temperatures on a silicon wafer are given. When the XRD graphics were examined, it was observed that the same molybdenum oxide structure which is α-MoO$_3$ was formed at 350, 400, and 450°C, and the metallic molybdenum peak disappeared. It was observed that α-MoO$_3$ has the highest intensity at 400°C. Hence, the optimized temperature for in-situ heat treatment was chosen as 400°C.
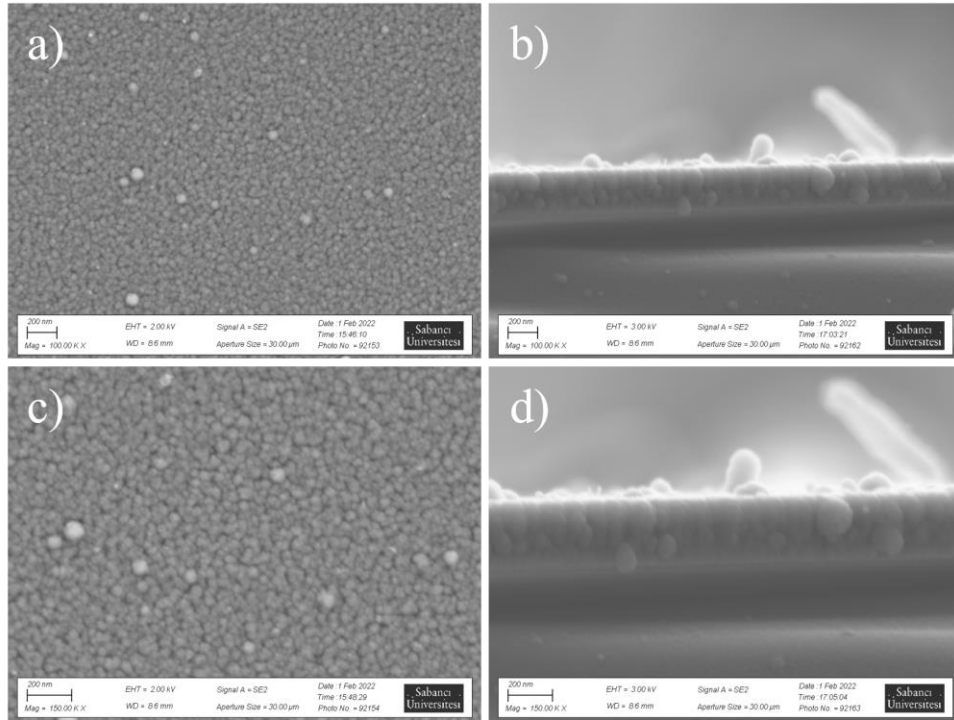
Figure 14. SEM images of reactively sputtered molybdenum oxide thin film at 400 °C
a) top-view 100000X b) cross-view 100000X c) top-view 150000X d) cross-view
150000X.

Figure 14 shows that it has been found that films magnified from SEM images have
small particle sizes and continuous films. Figure 5 shows (a, c) upper-section and (b, d)
side-section SEM images of molybdenum oxide films grown at 400°C for 10 minutes
on Si substrate. It has been observed that top-view SEM images show homogeneous
and smooth film morphology obtained and columnar growth was observed from the
cross-view images. The columnar type of growth was observed as mentioned in the
structure and zone model. When it is compared with the post-annealed samples, a
smoother surface can be observed from the side-view images.

3.4. Effect of Film Thickness on Film Composition and Microstructure
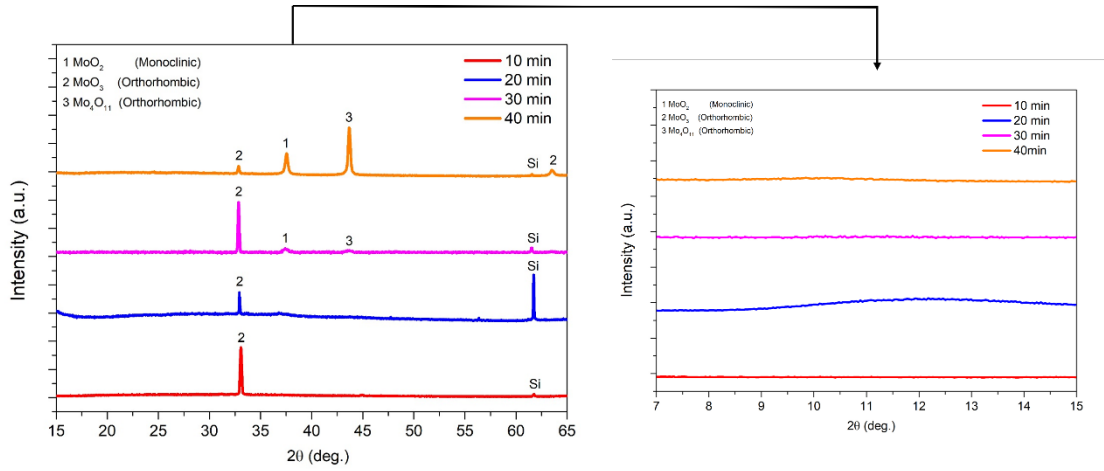
Figure 15. XRD spectra of thickness-dependent reactively sputtered molybdenum oxide thin film at 400°C.

XRD spectra of thin films deposited by in-situ heat treatment reactive rf sputtering technique using elemental Mo sputtering target are given in Figure (12). In order to determine the crystalline structure and phases of thin films grown on Si [001] substrates, XRD θ/2θ measurements were performed in the range of 2θ=5°-65°. As seen in Figure 1, all investigated films were crystalized in α-MoO$_3$ with a lattice constant of a=3.966, b=13.88, c=3.703 Å, β-MoO$_2$, and γ-Mo$_4$O$_{11}$ crystal structures. (JCPDS card no: 05-0507, 33-0929, 76-1683 respectively.) XRD pattern of 10 minutes of deposited film shows that the α-MoO3 thin film has a highly textured nature with a 2θ peak at 33.065° corresponding to (101) plane. The average crystallite size was calculated by the Scherrer equation for each deposited film.

$$B(2\theta) = \frac{K\lambda}{L\cos(\theta)}$$

(1)

B is the average crystallite size corresponding to the 2θ angle, K is proportionality constant, λ is the wavelength of the cupper K$_\alpha$ X-Ray photon, L is the full width of half maximum (FWHM), and θ is the angle of the pattern.
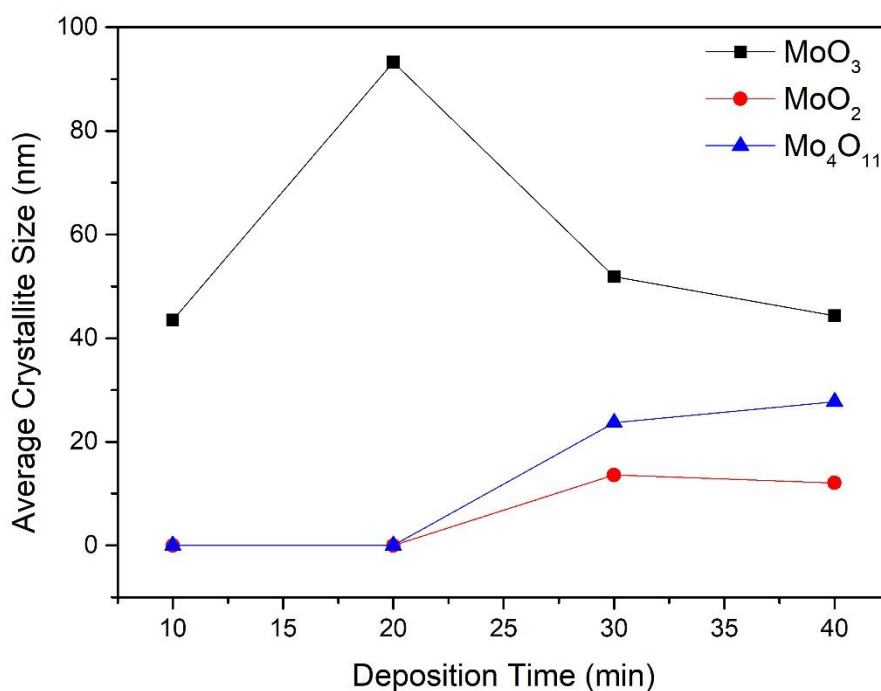
Figure 16. Average crystallite size graph as a function of deposition time.

According to the Scherrer equation, the average crystallite size of 10 minutes of the deposited film was 43nm. The peak position and angle of incidence of 20 minutes of the deposited thin film were the same as the 10 minutes of the deposited film. However, the average crystallite size was 93.27nm. The nanostructured sizes are getting higher with the increase in deposition time. As the deposition time increases to 30 and 40 minutes, the thin films start to lose their highly textured nature, and other molybdenum compounds start to form with high crystallite size for the dominant phase. The increase in crystallite size can be associated with both increasing film thickness and the longer in-situ heat treatment during the deposition. In 30 and 40 minutes, the average crystallite size starts to decrease while the formation of other compounds.
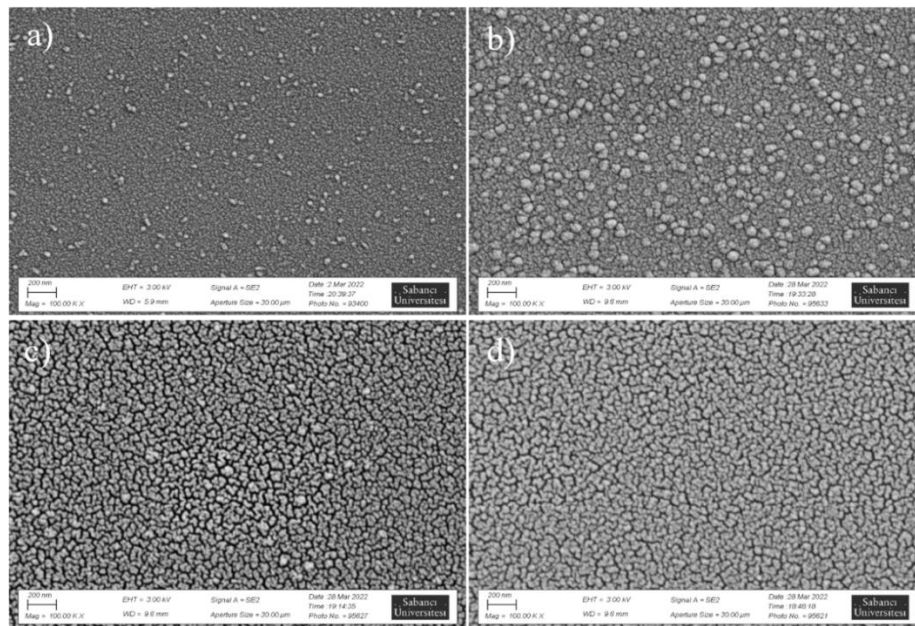
Figure 17. Top-view SEM images magnified at 100000X of reactively sputtered molybdenum oxide thin films at different deposition times a) 10 minutes b) 20 minutes c) 30 minutes d) 40 minutes.

Figure 17 shows upper-section SEM images of reactively sputtered molybdenum oxide thin films at different times. It has been found that films magnified for 20 minutes from SEM images have larger particle sizes compared to films magnified for 10 minutes. It is observed that porous structures are formed in the films grown for 30 and 40 minutes. Just by increasing the deposition time, the film thickness increases while the co-existence of the other Mo-O phases starts to appear and change the morphology. Long deposition time means exposing the samples to heat long time as well. The observed increase in the nanostructured size can be associated with the longer in-situ heat treatment of the samples during the deposition. Thicker samples are exposed longer time to heat in order to form grain growth. In conclusion, homogeneous and continuous films of molybdenum oxide were obtained.
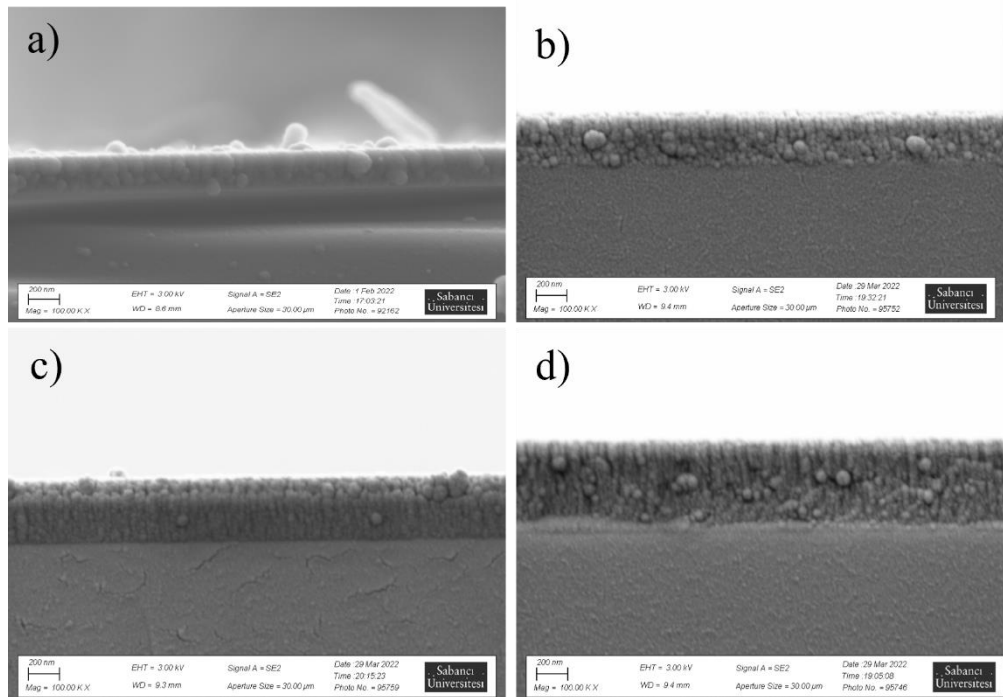
Figure 18. Cross-view SEM images magnified at 100000X of reactively sputtered molybdenum oxide thin films at different deposition times a) 10 minutes b) 20 minutes c) 30 minutes d) 40 minutes.

Figure 18 specifies that molybdenum oxide thin films grow columnar as stated in the structure zone model in the introduction section. As it seems in the images, the surface is quite smooth and clear. Therefore, the thicknesses of the films were determined by these cross-view SEM images. The thicknesses of the films for 10 to 40 minutes are measured at 120, 220, 335, and 450 nm. The film composition was tuned to α-MoO$_3$ up to about 335 nm according to the XRD spectrum.

3.5. Thickness Effect on Optical, Defect Concentration and Electrical Analysis

A technique for optical analysis called spectroscopic ellipsometry (SE) depends on how differently light is polarized when it is reflected from a planar surface. His method makes it possible to ascertain the optical characteristics of thin films that are influenced by parameters such as composition, thickness, porosity, or any other. The measured data can be used to create single or multilayer films with thicknesses ranging from a few nanometers to microns by fitting the data to a physical model of the structure. For uniform films that offer better reflection.

The Refractive index determines the path that light encounters before being bent inside the material. The critical angle for total internal reflection, the intensity, and Brewster's angle are all determined by the refractive indices, as well as the amount of light that is reflected when it reaches the interface [98].
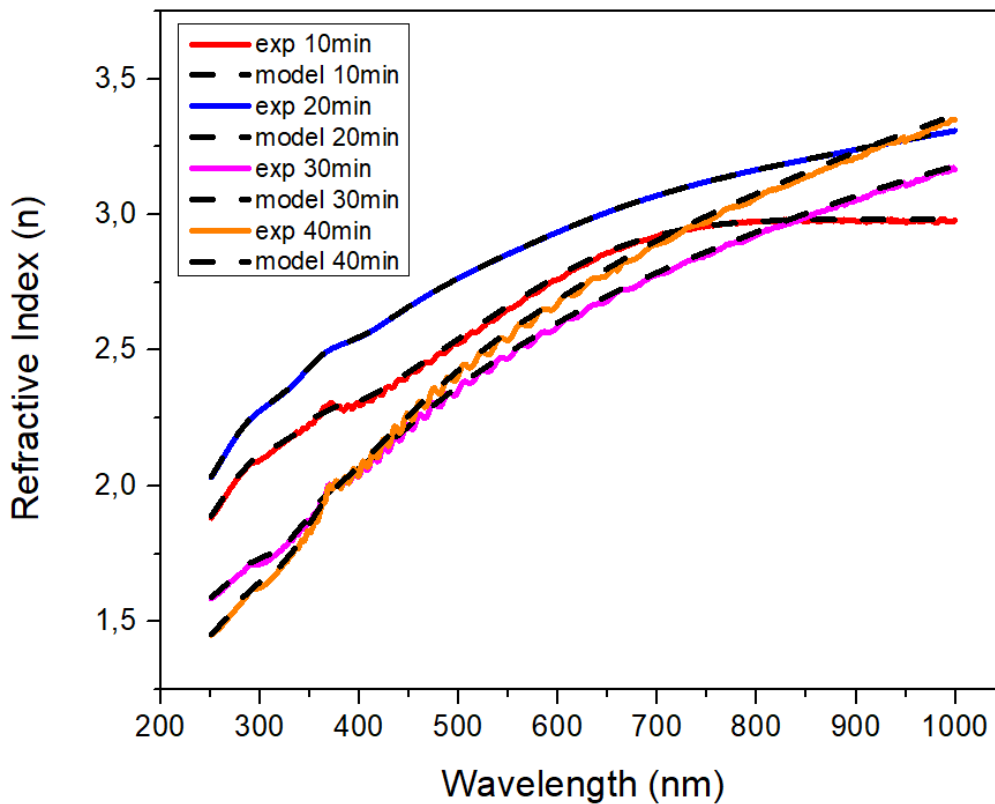
Figure 19. Refractive index graph as a function of wavelength by ellipsometry.

Figure 19 demonstrates the refractive index of the thin films deposited by RF magnetron sputtering. The values in the range from 1.5 to 3.2. The maxima point of the refractive index might be indicated by the inhomogeneities in the film structure. The structure of the films is formed by crystalline phases. The reason for this could be the high deposition rates during the deposition. In addition, substrate temperature might influence the refractive index due to enhancing the film density. Different values of the refractive index for each sample can be attributed to the thickness of the films. This behavior can be influenced by high crystallinity, the roughness of the surface, crystallite size, and defect concentration.
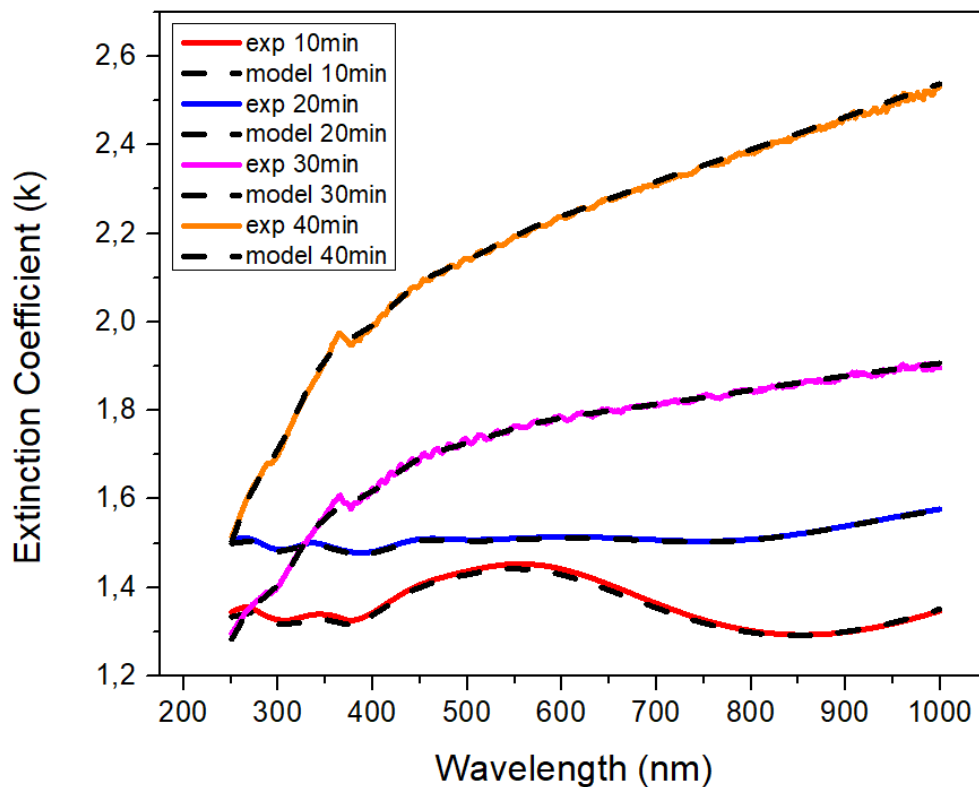
Figure 20. Extinction Coefficient graph as a function of wavelength by ellipsometry.

Figure 20 shows the extinction coefficient as a function of the wavelength plot for the same thin films. The k value gives the absorption of the light through the film. The maxima of the extinction coefficient indicate the presence of proper-type defects inside the film. In the plot, the extinction coefficient of each film has a higher k value than 1

which indicates the absorbance of the films is high. Extinction coefficient measurement is highly sensitive in lower thicknesses.

The absorption coefficient can be calculated by the extinction coefficient with the formula below:

$$\alpha = \frac{4\pi k}{\lambda} \tag{2}$$

In the formula, k is the extinction coefficient, and λ is the wavelength. The general literature review and the result we've found in the absorption coefficient spectrum are in an agreement that MoO_3 has a direct band gap. The direct band gap can be calculated by the equation below:

$$(\alpha h\upsilon)^n = A(h\upsilon - E_g) \tag{3}$$

α is the absorption coefficient, h is Planck's constant, υ is the frequency of the photon, n is the nature of electron transition, A is the probability parameter for the transition, and E_g is the band gap. When n is equal to 2, the direct band gap is calculated by the Tauc plot. The $(\alpha h\upsilon)^{1/2}$ have no linear behavior which suggests that molybdenum oxide thin films deposited by RF reactive sputtering.
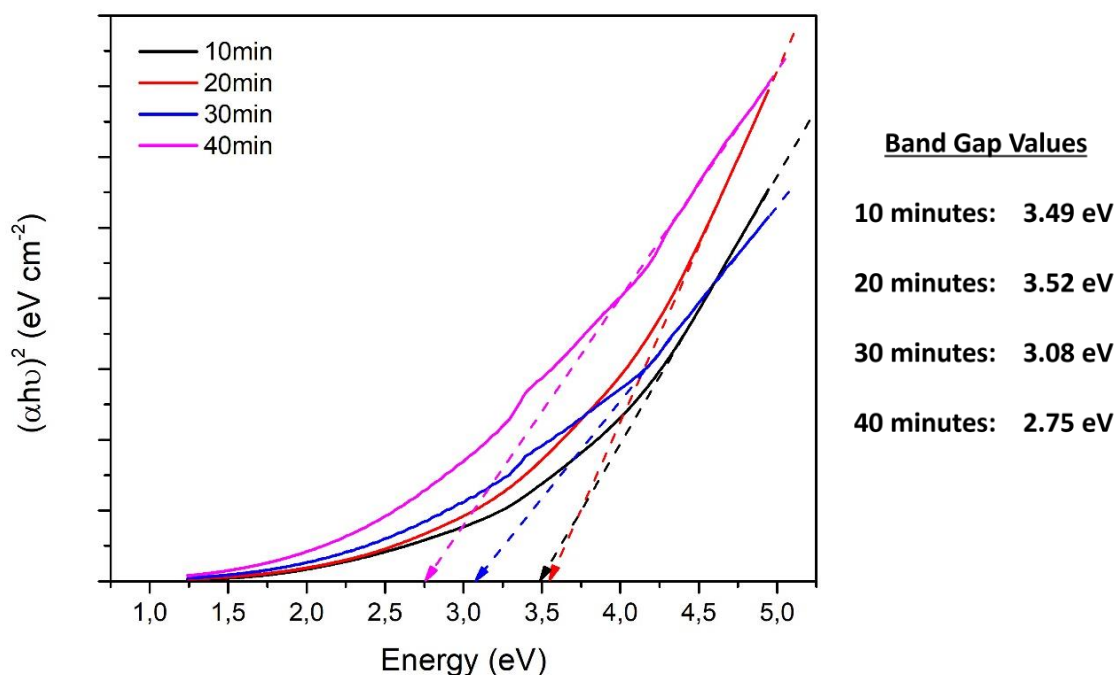
Figure 21. Band gap calculation by Tauc plot.

Figure 21 is presented for the variation of $(\alpha h\upsilon)^2$ as a function of the energy of MoO$_3$ thin films prepared at different deposition times. The band gap is estimated from the extrapolation of the linear part of the curve intersecting with the energy axis. The optical band gap of the thin films is found in the range of 2.75 to 3.52 eV. 20 minutes sample has a slightly higher band gap than 10 minutes sample. This might be attributed to the partial filling of oxygen vacancies formed while the deposition. The band gap reduces with the increase in the deposition time to 30 and 40 minutes. The reason for the decrease can be linked to the oxygen vacancies that can capture the electron from the conduction band by acting like a donor center. Moreover, the dominant phase becomes a molybdenum oxide compound with oxygen deficiency and molybdenum tends to grow oxygen deficient as the deposition time is prolonged according to the XRD results. Sub-stoichiometric molybdenum oxide films show more metallic characteristics resulting in a reduction in the band gap.

Photoluminescence measurement was performed at the excitation wavelength of 250 nm which is 4.97 eV. The excitation wavelength is higher than the band gap energy to excite an electron from the valence band to the conduction band directly, yet it is possible to excite the electron to the localized level within the forbidden gap. The intensity of PL is affected by many parameters may rise from the sample properties or device condition. Based on this information, it is known that geometry, nanostructure type, and substrate can affect the photoluminescence intensity drastically. The change in the confinement of carriers in tiny volumes of differently shaped nanostructures may be the cause of the morphology-dependent PL behavior [99]. The locations of the PL bands may change depending on the makeup of the substrates. Additionally, the high surface-to-volume ratio, high lattice mismatch, and surface roughness of the film all contribute to variations in PL density. Because materials having a high surface-to-volume ratio are more likely to absorb incoming light, it is expected that their PL densities will be higher [100]. The increase in surface area, which enables high absorption of incoming UV light, may be the cause of the rise in PL intensity with an increase in porosity and roughness. In contrast to a smooth film, which generates specular reflection, a rough film may let the excitation beam to reflect onto a different region of the film surface, resulting in a more efficient utilization of the excitation energy and hence superior PL intensity. Due to a combination of total internal reflection and incident light reflection, the films with modest surface roughness exhibit somewhat low PL intensity [99].
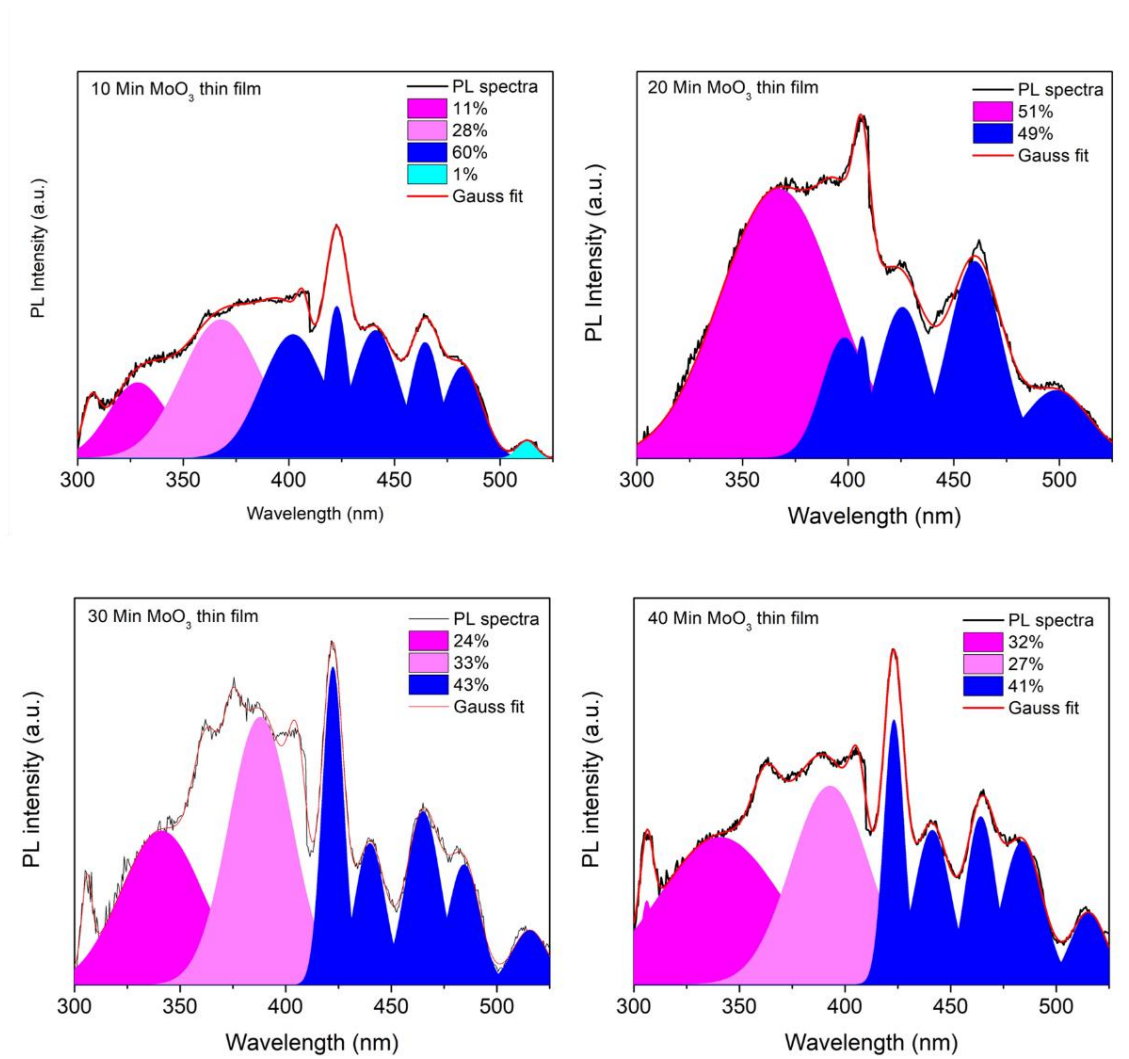
Figure 22. Photoluminescence spectra of reactively sputtered molybdenum oxide thin films at different deposition times a) 10 minutes b) 20 minutes c) 30 minutes d) 40 minutes.

Figure 22 shows emissions in the range of 300-550 nm. The calculated band gap of the films from the Tauc plot was in the range of 2.7-3.6 eV. Beyond it, especially in the UV range might be attributed to the lattice imperfections or it can be linked to the radiative decay of self-trapped excitons. Lattice imperfections can be oxygen vacancies or more complex defect centers. Formation of the oxygen vacancies lowers the oxidation state of Mo which is shown as Mo^{6+} to Mo^{5+} [101], [102]. Because an oxygen vacancy can distort MoO_6 octahedra by pushing a Mo atom in the direction of the terminal oxygens, oxygen vacancies play a significant role in the PL emission. This lattice disruption

determines the energy position of the defect states regarding the valence band and the conduction band. The crystal field effect causes the core Mo ion's d levels to separate into distinct energy levels in the deformed octahedra of α-MoO$_3$. Excitonic emission bands are created when these levels change due to stimulation. Accordingly, the Mo^{5+} d-d band transition of a severely deformed polyhedron (Mo-O) in an octahedral crystal field may be responsible for the transitions in the visible area in the crystal field model [103], [104].

Table 6 Percentage of UV and blue light emission from the time-variant samples

Material	Near band emissions %	Blue light emissions %
10 Min MoO$_3$ Thin film	39	61
20 Min MoO$_3$ Thin film	51	49
30 Min MoO$_3$ Thin film	57	43
40 Min MoO$_3$ Thin film	59	41
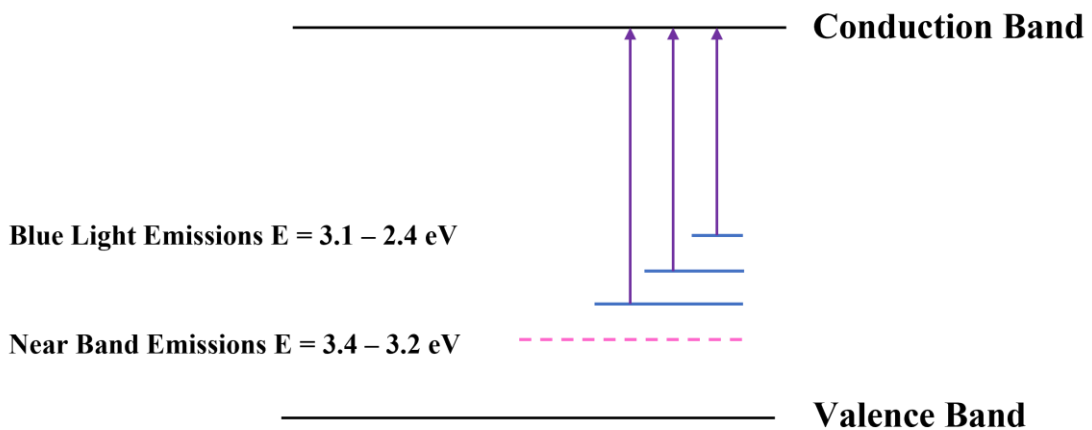
Figure 23. Illustration of the emission states.

As shown in the Table 6 and emission states, blue light emission decrease with the deposition time increase was observed. On the other hand, UV light emission increases with the thickness of the films. This can be stated that the defect structures possibly oxygen vacancies increase with the UV light emission and reduces with the blue light

emission. As a result, it can be attributed to the oxidation state of oxygen. Correspondingly, the amount of oxygen vacancies increases according to the PL results which is consistent with the band gap calculations from the Tauc plot. The increased amount of oxygen vacancies decrease the band gap and the 40 minutes sample shows more metallic property which explains the high value of the imaginary part of the dielectric function which is the extinction coefficient.

One of the most sophisticated methods for identifying paramagnetic point defects in solid-state materials including metal oxides, carbides, and borides is EPR spectroscopy. The local configuration and electrical characteristics of unpaired electrons, which are intimately connected to spin-orbit coupling and heavily dependent on the value of g-factors, may be learned from EPR in a profound and beneficial way. Here, X-band (9.64 GHz) continuous wave EPR spectroscopy was employed at room temperature to understand the roles of defect structures in the performance of MoO_3 thin films. The EPR intensity as a function of the applied Magnetic field is plotted in Figure 24 and g-factors are calculated by using the following equation:

$$hv = g\beta B$$

(4)

where h is the plank constant, v is the applied microwave frequency, β is the Bohr Magneton and B is the applied Magnetic field.
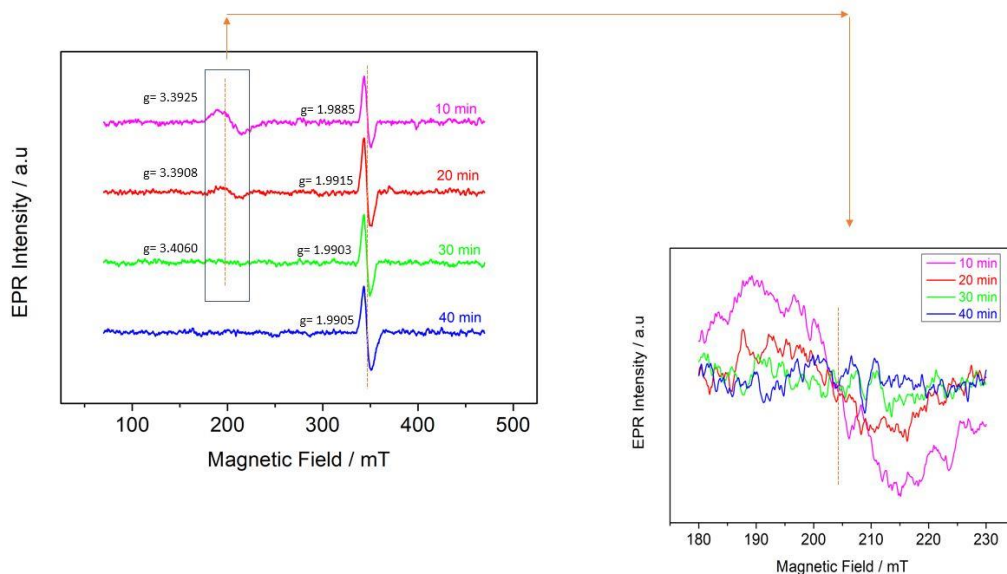
Figure 24. EPR spectra of reactively sputtered molybdenum oxide thin films at different deposition times.

Although many studies are reported for MoO_3, there are not studies that focused on the effect of molybdenum ion EPR measurements. There are two types of signals observed from the EPR measurement. Based on the g values given in the literature, the signal with $g_\perp$=2.09 and $g_\parallel$=2.00 was temporarily assigned to O^- [105] which is localized in the coordination sphere of Mo^{+6} ions [106] and the g values of 2.0023 are the signal of a free electron [107]. In figure 20, the signal of g = 1.9885 was observed which corresponds to the MoO_3 lattice's hexa-coordinated MoO_6 octahedra having an oxygen vacancy, which is where this signal is connected to Mo^{5+} [107]. It was observed that as the deposition time increased, the peak starts to broaden which is linked to the several overlapping signals according to the reports and although, the signal at around g = 1.98 has mentioned to be attributed to the Mo^{5+} species, the signal may not be resolved due to the frequency limitation. Besides, as the deposition time increases UV light emission brings about the defects especially oxygen vacancies in the sample according to the PL results. In this case, broader peaks at 40 minutes sample may have higher oxygen vacancies concentration that EPR couldn't resolve. In addition, the signal with a g factor is 3.3925 can be attributed to the Si wafer and as the thickness increases, the signal from the Si wafer disappears.
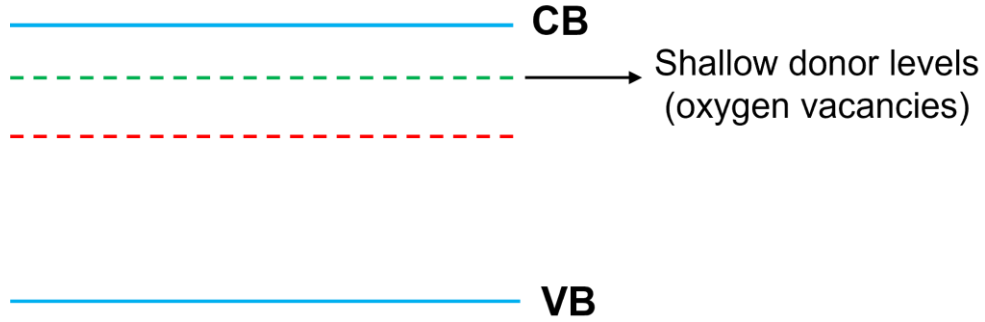
Figure 25 Schematic representation of shallow donor levels (oxygen vacancies).

In this figure, since the oxygen vacancies are assigned to shallow donors and they are attributed to the singly ionized oxygen vacancies, these shallow donor levels start to appear just below the conduction band edge. When the concentration of oxygen vacancies is high, shallow donor levels become more delocalized and overlap with the conduction band edge. This overlap results to the band gap narrowing and explains the band gap decrease according to the data obtained from Tauc plot.

PL and EPR results verified the oxygen vacancies inside the films. These oxygen vacancies should have an effect on the sheet resistance as well. Therefore, the electrical properties of grown molybdenum oxide thin films by reactive sputtering on a silicon wafer at different time intervals were analyzed by a 4-Point Probe in order to investigate the sheet resistance. Sheet resistance has an important role in the device's performance. For evaluating the doped areas on c-Si wafers, sheet resistance measurements are highly preferred to be performed. In addition, it is used to characterize the doping processes which is made of ion implantation, laser doping or thermal diffusion [108]–[111]. Sheet resistance can be calculated by the equations below.

$$\rho = \frac{\pi t}{\ln 2}\left(\frac{V}{I}\right)$$

$$R_s = \frac{\rho}{t} \tag{5}$$
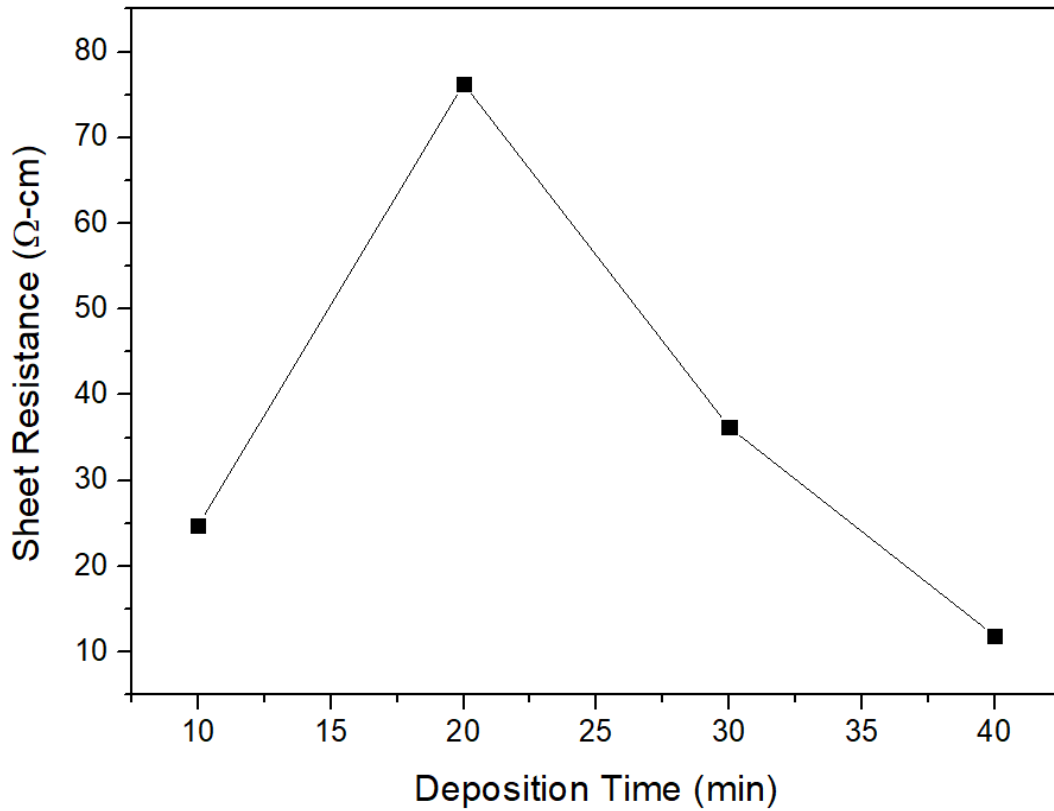
Figure 26. Sheet resistance graph as a function of deposition time by 4-point probe.

According to the Figure 25, the sheet resistance first starts to increase by the thickness, after it starts to decrease. 20 minutes sample has slightly higher value in sheet resistance due to the partial filling of the oxygen vacancies during the deposition. By the increasing deposition time, the concentration of the oxygen vacancies becomes higher which means there are more-free electron inside the film. In this way, the conductance of the film gets higher with the lower value in the sheet resistance. The higher conductance is important for the semiconductors. Enhancing the conductance of the films by creating oxygen vacancies during the deposition allows the films to be used in the electronic device applications.

4. CONCLUSION

MoO$_3$ has been successfully grown by reactive magnetron sputtering on [001] Si substrate. Their crystallinity increased by applying in-situ heat treatment. The structural, morphological, and electrical properties of MoO$_3$ films were investigated by several characterization techniques besides the effect of the correlation between the thickness and deposition parameters on the defect concentration. Films deposited at deposition time shorter than 40 minutes have a α-MoO$_3$ dominated crystal. In contrast, the film deposited at 40 minutes consists mainly of a dominant β-MoO$_2$ phase structure as well as consisting of α-MoO$_3$ and γ-Mo$_4$O$_{11}$ structures. The formed films in the system molybdenum oxide compound are therefore interesting materials for a variety of optical and electrical applications such as gas sensor, storage devices or micro batteries. Since the structure and properties of the deposited MoO$_3$ thin films were modified by varying the deposition period as well as the thickness. These discoveries may also be useful for improving the structure and characteristics of other metal oxide thin films through suitable adjustment of film thickness and defect engineering principles.

REFERENCES

[1]   N. Ramgir *et al.*, "Metal oxide nanowires for chemiresistive gas sensors: Issues, challenges and prospects," *Colloids Surf A Physicochem Eng Asp*, vol. 439, pp. 101–116, Dec. 2013, doi: 10.1016/J.COLSURFA.2013.02.029.

[2]   J. Henzie, J. E. Barton, C. L. Stender, and T. W. Odom, "Large-Area Nanoscale Patterning: Chemistry Meets Fabrication," *Acc Chem Res*, vol. 39, no. 4, pp. 249–257, Jan. 2006, doi: 10.1021/ar050013n.

[3]   C. M. Hangarter, M. Bangar, A. Mulchandani, and N. v. Myung, "Conducting polymer nanowires for chemiresistive and FET-based bio/chemical sensors," *J Mater Chem*, vol. 20, no. 16, pp. 3131–3140, 2010, doi: 10.1039/b915717d.

[4]   A. I. Hochbaum and P. Yang, "Semiconductor Nanowires for Energy Conversion," *Chem Rev*, vol. 110, no. 1, pp. 527–546, Oct. 2009, doi: 10.1021/cr900075v.

[5]   R. K. Joshi, Q. Hu, F. Alvi, N. Joshi, and A. Kumar, "Au Decorated Zinc Oxide Nanowires for CO Sensing," *The Journal of Physical Chemistry C*, vol. 113, no. 36, pp. 16199–16202, Aug. 2009, doi: 10.1021/jp906458b.

[6]   W.-K. Hong *et al.*, "Tunable Electronic Transport Characteristics of Surface-Architecture-Controlled ZnO Nanowire Field Effect Transistors," *Nano Lett*, vol. 8, no. 3, pp. 950–956, Feb. 2008, doi: 10.1021/nl0731116.

[7]   J. Huang and Q. Wan, "Gas Sensors Based on Semiconducting Metal Oxide One-Dimensional Nanostructures," *Sensors*, vol. 9, no. 12, pp. 9903–9924, Dec. 2009, doi: 10.3390/s91209903.

[8]   "Small - 2010 - Ramgir - Nanowire-Based Sensors.pdf."

[9]   J. de Oliveira Mota *et al.*, "Environmental monitoring program to support food microbiological safety and quality in food industries: A scoping review of the research and guidelines," *Food Control*, vol. 130, p. 108283, Dec. 2021, doi: 10.1016/J.FOODCONT.2021.108283.

[10] V. Nirupama, K. R. Gunasekhar, B. Sreedhar, and S. Uthanna, "Effect of oxygen partial pressure on the structural and optical properties of dc reactive magnetron sputtered molybdenum oxide films," *Current Applied Physics*, vol. 10, no. 1, pp. 272–278, 2010, doi: 10.1016/j.cap.2009.06.005.

[11] P. Fathi, N. C. Karmakar, M. Bhattacharya, and S. Bhattacharya, "Potential Chipless RFID Sensors for Food Packaging Applications: A Review," *IEEE Sens J*, vol. 20, no. 17, pp. 9618–9636, 2020, doi: 10.1109/JSEN.2020.2991751.

[12] H. Yousefi, H. M. Su, S. M. Imani, K. Alkhaldi, C. D. Filipe, and T. F. Didar, "Intelligent Food Packaging: A Review of Smart Sensing Technologies for Monitoring Food Quality," *ACS Sens*, vol. 4, no. 4, pp. 808–821, 2019, doi: 10.1021/acssensors.9b00440.

[13] N. Funazaki *et al.*, "Application of semiconductor gas sensor to quality control of meat freshness in food industry," *Sens Actuators B Chem*, vol. 25, no. 1–3, pp. 797–800, Apr. 1995, doi: 10.1016/0925-4005(95)85177-1.

[14] S. Marín, A. J. Ramos, and V. Sanchis, "Comparison of methods for the assessment of growth of food spoilage moulds in solid substrates," *Int J Food Microbiol*, vol. 99, no. 3, pp. 329–341, Apr. 2005, doi: 10.1016/J.IJFOODMICRO.2004.10.035.

[15] D. Kohl, "Function and applications of gas sensors," *J Phys D Appl Phys*, vol. 34, no. 19, pp. R125–R149, Oct. 2001, doi: 10.1088/0022-3727/34/19/201.

[16] G. F. Fine, L. M. Cavanagh, A. Afonja, and R. Binions, "Metal Oxide Semi-Conductor Gas Sensors in Environmental Monitoring," *Sensors*, vol. 10, no. 6, pp. 5469–5502, Jun. 2010, doi: 10.3390/s100605469.

[17] N. Ramgir *et al.*, "Metal oxide nanowires for chemiresistive gas sensors: Issues, challenges and prospects," *Colloids Surf A Physicochem Eng Asp*, vol. 439, pp. 101–116, Dec. 2013, doi: 10.1016/J.COLSURFA.2013.02.029.

[18] A. Szekeres, T. Ivanova, and K. Gesheva, "Spectroscopic ellipsometry study of CVD molybdenum oxide films: Effect of temperature," *Journal of Solid State Electrochemistry*, vol. 7, no. 1, pp. 17–20, 2002, doi: 10.1007/s10008-002-0285-4.

[19] S. R. Meher, "Transition metal oxide-based materials for visible-light-photocatalysis," *Nanostructured Materials for Visible Light Photocatalysis*, pp. 153–183, Jan. 2022, doi: 10.1016/B978-0-12-823018-3.00021-X.

[20] C. Imawan, H. Steffes, F. Solzbacher, and E. Obermeier, "A new preparation method for sputtered MoO3 multilayers for the application in gas sensors," *Sens Actuators B Chem*, vol. 78, no. 1–3, pp. 119–125, 2001, doi: 10.1016/S0925-4005(01)00801-2.

[21] S. Barazzouk, R. P. Tandon, and S. Hotchandani, "MoO3-based sensor for NO, NO2 and CH4 detection," *Sens Actuators B Chem*, vol. 119, no. 2, pp. 691–694, Dec. 2006, doi: 10.1016/J.SNB.2006.01.026.

[22] Y. Liu, S. Yang, Y. Lu, N. v. Podval'naya, W. Chen, and G. S. Zakharova, "Hydrothermal synthesis of h-MoO3 microrods and their gas sensing properties to ethanol," *Appl Surf Sci*, vol. 359, pp. 114–119, Dec. 2015, doi: 10.1016/J.APSUSC.2015.10.071.

[23] A. K. Prasad, D. J. Kubinski, and P. I. Gouma, "Comparison of sol–gel and ion beam deposited MoO3 thin film gas sensors for selective ammonia detection," *Sens Actuators B Chem*, vol. 93, no. 1–3, pp. 25–30, Aug. 2003, doi: 10.1016/S0925-4005(03)00336-8.

[24] Y. X. Li *et al.*, "Nano structured molybdenum oxide gas sensors," *Proceedings of IEEE Sensors*, pp. 232–234, 2006, doi: 10.1109/ICSENS.2007.355764.

[25] A. Bouzidi, N. Benramdane, H. Tabet-Derraz, C. Mathieu, B. Khelifa, and R. Desfeux, "Effect of substrate temperature on the structural and optical properties of MoO3 thin films prepared by spray pyrolysis technique," *Mater Sci Eng B Solid State Mater Adv Technol*, vol. 97, no. 1, pp. 5–8, 2003, doi: 10.1016/S0921-5107(02)00385-9.

[26] Y. Zhao, A. M. Nardes, and K. Zhu, "Effective hole extraction using MoO$_x$ -Al contact in perovskite CH$_3$ NH$_3$ PbI$_3$ solar cells," *Appl Phys Lett*, vol. 104, no. 21, p. 213906, May 2014, doi: 10.1063/1.4880899.

[27] J. Bullock, A. Cuevas, T. Allen, and C. Battaglia, "Molybdenum oxide MoO $_x$: A versatile hole contact for silicon solar cells," *Appl Phys Lett*, vol. 105, no. 23, p. 232109, Dec. 2014, doi: 10.1063/1.4903467.

[28] A. L. F. Cauduro *et al.*, "Crystalline Molybdenum Oxide Thin-Films for Application as Interfacial Layers in Optoelectronic Devices," *ACS Appl Mater Interfaces*, vol. 9, no. 8, pp. 7717–7724, 2017, doi: 10.1021/acsami.6b14228.

[29] G. Eranna, B. C. Joshi, D. P. Runthala, and R. P. Gupta, "Oxide materials for development of integrated gas sensors - A comprehensive review," *Critical Reviews in Solid State and Materials Sciences*, vol. 29, no. 3–4, pp. 111–188, 2004, doi: 10.1080/10408430490888977.

[30] D. Manno, A. Serra, M. di Giulio, G. Micocci, and A. Tepore, "Physical and structural characterization of tungsten oxide thin films for NO gas detection," *Thin Solid Films*, vol. 324, no. 1–2, pp. 44–51, 1998, doi: 10.1016/S0040-6090(97)01205-4.

[31] C. M. Lampert, "Electrochromic materials and devices for energy efficient windows," *Solar Energy Materials*, vol. 11, no. 1–2, pp. 1–27, 1984, doi: 10.1016/0165-1633(84)90024-8.

[32] Y. Gong, Y. Dong, B. Zhao, R. Yu, S. Hu, and Z. Tan, "Diverse applications of MoO3 for high performance organic photovoltaics: Fundamentals, processes and optimization strategies," *J Mater Chem A Mater*, vol. 8, no. 3, pp. 978–1009, 2020, doi: 10.1039/c9ta12005j.

[33] X. Wen Lou and H. Chun Zeng, "Complex α-MoO3 Nanostructures with External Bonding Capacity for Self-Assembly," *J Am Chem Soc*, vol. 125, no. 9, pp. 2697–2704, Feb. 2003, doi: 10.1021/ja029086h.

[34] K. Kalantar-Zadeh *et al.*, "Synthesis of nanometre-thick MoO3 sheets," *Nanoscale*, vol. 2, no. 3, pp. 429–433, 2010, doi: 10.1039/b9nr00320g.

[35] S. S. Sunu, E. Prabhu, V. Jayaraman, K. I. Gnanasekar, T. K. Seshagiri, and T. Gnanasekaran, "Electrical conductivity and gas sensing properties of MoO3," *Sens Actuators B Chem*, vol. 101, no. 1–2, pp. 161–174, Jun. 2004, doi: 10.1016/J.SNB.2004.02.048.

[36] D. Dhawan, S. Bhargava, J. Tardio, W. Wlodarski, and K. Kalantar-Zadeh, "Gold Coated Nanostructured Molybdenum Oxide Mercury Vapour Quartz Crystal Microbalance Sensor," *Sens Lett*, vol. 6, no. 1, pp. 231–236, Feb. 2008, doi: 10.1166/sl.2008.031.

[37] D. di Yao, J. Z. Ou, K. Latham, S. Zhuiykov, A. P. O'Mullane, and K. Kalantar-Zadeh, "Electrodeposited α- And β-phase MoO 3 films and investigation of their gasochromic properties," *Cryst Growth Des*, vol. 12, no. 4, pp. 1865–1870, 2012, doi: 10.1021/cg201500b.

[38] Y. Zhu *et al.*, "Nanostructured MoO3 for efficient energy and environmental catalysis," *Molecules*, vol. 25, no. 1, pp. 1–26, 2020, doi: 10.3390/molecules25010018.

[39] K. Inzani, M. Nematollahi, F. Vullum-Bruer, T. Grande, T. W. Reenaas, and S. M. Selbach, "Electronic properties of reduced molybdenum oxides," *Physical Chemistry Chemical Physics*, vol. 19, no. 13, pp. 9232–9245, 2017, doi: 10.1039/c7cp00644f.

[40] A. A. Mane and A. v. Moholkar, "Orthorhombic MoO3 nanobelts based NO2 gas sensor," *Appl Surf Sci*, vol. 405, pp. 427–440, May 2017, doi: 10.1016/J.APSUSC.2017.02.055.

[41] O. de Melo *et al.*, "Optical and electrical properties of MoO2 and MoO3 thin films prepared from the chemically driven isothermal close space vapor transport technique," *Journal of Physics Condensed Matter*, vol. 31, no. 29, 2019, doi: 10.1088/1361-648X/ab18e2.

[42] D. J. Borah, A. T. T. Mostako, P. K. Saikia, and P. Dutta, "Effect of thickness and post deposition annealing temperature on the structural and optical properties of thermally evaporated molybdenum oxide films," *Mater Sci Semicond Process*, vol. 93, pp. 111–122, Apr. 2019, doi: 10.1016/J.MSSP.2018.12.038.

[43] "Investigation of hole injection enhancement by MoO 3 buffer layer in organic light emitting diodes," *J Appl Phys*, vol. 114, no. 24, p. 244505, Dec. 2013, doi: 10.1063/1.4852835.

[44] H. Simchi, B. E. McCandless, T. Meng, J. H. Boyle, and W. N. Shafarman, "Characterization of reactively sputtered molybdenum oxide films for solar cell application," *J Appl Phys*, vol. 114, no. 1, p. 013503, Jul. 2013, doi: 10.1063/1.4812587.

[45] P. S. Wang, Y. Y. Lo, W. H. Tseng, M. H. Chen, and C. I. Wu, "Enhancing the incorporation compatibility of molybdenum oxides in organic light emitting diodes with gap state formations," *J Appl Phys*, vol. 114, no. 6, 2013, doi: 10.1063/1.4817423.

[46] Y. Zhao *et al.*, "Preparation of MoO3 nanostructures and their optical properties," *Journal of Physics Condensed Matter*, vol. 15, no. 35, 2003, doi: 10.1088/0953-8984/15/35/101.

[47] V. D. Das and D. Karunakaran, "Semiconducting behavior of Ag $_2$ Te thin films and the dependence of band gap on thickness," *J Appl Phys*, vol. 54, no. 9, pp. 5252–5255, Sep. 1983, doi: 10.1063/1.332753.

[48] J. C. Slater, "Barrier Theory of the Photoconductivity of Lead Sulfide," *Physical Review*, vol. 103, no. 6, pp. 1631–1644, Sep. 1956, doi: 10.1103/PhysRev.103.1631.

[49] P. Maiti, P. Guha, R. Singh, J. K. Dash, and P. v. Satyam, "Optical band gap, local work function and field emission properties of MBE grown β-MoO3 nanoribbons," *Appl Surf Sci*, vol. 476, pp. 691–700, May 2019, doi: 10.1016/J.APSUSC.2019.01.124.

[50] R. Tokarz-Sobieraj, K. Hermann, M. Witko, A. Blume, G. Mestl, and R. Schlögl, "Properties of oxygen sites at the MoO3(010) surface: Density functional theory cluster studies and photoemission experiments," *Surf Sci*, vol. 489, no. 1–3, pp. 107–125, 2001, doi: 10.1016/S0039-6028(01)01169-4.

[51] R. Coquet and D. J. Willock, "The (010) surface of," vol. 3, no. 010, pp. 3819–3828, 2005.

[52] "(2013, Adv Funct. Mat) Metal and Metal-Oxide Interfaces How Metal Contacts Affect the Work Function and Band Structure of MoO3.pdf."

[53] E. Brocławik and J. Haber, "SCF-SW-Xα calculations of the removal of oxygen from oxide surfaces by vacancy formation and crystallographic shear mechanisms," *J Catal*, vol. 72, no. 2, pp. 379–382, Dec. 1981, doi: 10.1016/0021-9517(81)90023-3.

[54] J. Meyer *et al.*, "Metal oxide induced charge transfer doping and band alignment of graphene electrodes for efficient organic light emitting diodes," *Sci Rep*, vol. 4, pp. 1–7, 2014, doi: 10.1038/srep05380.

[55] P. R. Huang, Y. He, C. Cao, and Z. H. Lu, "Impact of lattice distortion and electron doping on α-MoO3 electronic structure," *Sci Rep*, vol. 4, pp. 1–7, 2014, doi: 10.1038/srep07131.

[56] S. Bandaru, G. Saranya, N. J. English, C. Yam, and M. Chen, "Tweaking the electronic and optical properties of a-MoO3 by sulphur and selenium doping - A density functional theory study," *Sci Rep*, vol. 8, no. 1, pp. 1–12, 2018, doi: 10.1038/s41598-018-28522-7.

[57] C. Battaglia *et al.*, "Hole Selective MoOx Contact for Silicon Solar Cells," *Nano Lett*, vol. 14, no. 2, pp. 967–971, Jan. 2014, doi: 10.1021/nl404389u.

[58] G. B. Smith, D. Golestan, and A. R. Gentle, "The insulator to correlated metal phase transition in molybdenum oxides," *Appl Phys Lett*, vol. 103, no. 5, p. 051119, Jul. 2013, doi: 10.1063/1.4817588.

[59] C. T. Tsai, D. S. Chuu, G. L. Chen, and S. L. Yang, "Studies of grain size effects in rf sputtered CdS thin films," *J Appl Phys*, vol. 79, no. 12, pp. 9105–9109, Jun. 1996, doi: 10.1063/1.362645.

[60] A. D. Compaan, C. N. Tabory, M. Shao, A. Fischer, Z. Feng, and R. G. Bohn, "Rf sputtering of CdTE and CdS for thin film PV," in *AIP Conference Proceedings*, 1994, vol. 306, pp. 329–334. doi: 10.1063/1.45762.

[61] S. Rondiya, A. Rokade, A. Funde, M. Kartha, H. Pathan, and S. Jadkar, "Synthesis of CdS thin films at room temperature by RF-magnetron sputtering and study of its structural, electrical, optical and morphology properties," *Thin Solid Films*, vol. 631, pp. 41–49, Jun. 2017, doi: 10.1016/J.TSF.2017.04.006.

[62] J. W. Choi, A. Bhupathiraju, M. A. Hasan, and J. M. Lannon, "Stoichiometry, morphology and structure of CdS layers grown on InP(1 0 0) from atomic sulfur beam generated from H2S gas and thermally evaporated Cd using molecular beam epitaxy," *J Cryst Growth*, vol. 255, no. 1–2, pp. 1–7, Jul. 2003, doi: 10.1016/S0022-0248(03)01150-3.

[63] F. R. White, A. H. Clark, M. C. Graf, and L. L. Kazmerski, "Growth of CuInSe $_2$ on CdS using molecular beam epitaxy," *J Appl Phys*, vol. 50, no. 1, pp. 544–545, Jan. 1979, doi: 10.1063/1.325624.

[64] S. Yilmaz, Y. Atasoy, M. Tomakin, and E. Bacaksiz, "Comparative studies of CdS, CdS:Al, CdS:Na and CdS:(Al–Na) thin films prepared by spray pyrolysis," *Superlattices Microstruct*, vol. 88, pp. 299–307, Dec. 2015, doi: 10.1016/J.SPMI.2015.09.021.

[65] S. Yilmaz, "The investigation of spray pyrolysis grown CdS thin films doped with flourine atoms," *Appl Surf Sci*, vol. 357, pp. 873–879, Dec. 2015, doi: 10.1016/J.APSUSC.2015.09.098.

[66] A. Slonopas *et al.*, "Growth mechanisms and their effects on the opto-electrical properties of CdS thin films prepared by chemical bath deposition," *Mater Sci Semicond Process*, vol. 52, pp. 24–31, Sep. 2016, doi: 10.1016/J.MSSP.2016.05.011.

[67] L. v. García, M. I. Mendivil, T. K. D. Roy, G. A. Castillo, and S. Shaji, "Laser sintering of magnesia with nanoparticles of iron oxide and aluminum oxide," *Appl Surf Sci*, vol. 336, pp. 59–66, May 2015, doi: 10.1016/J.APSUSC.2014.09.140.

[68] C. M. Dai, L. Horng, W. F. Hsieh, Y. T. Shih, C. T. Tsai, and D. S. Chuu, "High orientation CdS thin films grown by pulsed laser and thermal evaporation," *Journal of Vacuum Science & Technology A: Vacuum, Surfaces, and Films*, vol. 10, no. 3, pp. 484–488, May 1992, doi: 10.1116/1.578175.

[69] F. Iacomi, M. Purica, E. Budianu, P. Prepelita, and D. Macovei, "Structural studies on some doped CdS thin films deposited by thermal evaporation," *Thin*

Solid Films, vol. 515, no. 15, pp. 6080–6084, May 2007, doi: 10.1016/J.TSF.2006.12.091.

[70] B. Liu *et al.*, "Effects of deposition temperature and CdCl2 annealing on the CdS thin films prepared by pulsed laser deposition," *J Alloys Compd*, vol. 654, pp. 333–339, Jan. 2016, doi: 10.1016/J.JALLCOM.2015.08.247.

[71] H. Tao, Z. Jin, W. Wang, J. Yang, and Z. Hong, "Preparation and characteristics of CdS thin films by dip-coating method using its nanocrystal ink," *Mater Lett*, vol. 65, no. 9, pp. 1340–1343, May 2011, doi: 10.1016/J.MATLET.2011.01.077.

[72] P. J. Kelly and R. D. Arnell, "Magnetron sputtering: A review of recent developments and applications," *Vacuum*, vol. 56, no. 3, pp. 159–172, 2000, doi: 10.1016/S0042-207X(99)00189-X.

[73] S. M. Rossnagel, "Thin film deposition with physical vapor deposition and related technologies," *Journal of Vacuum Science & Technology A: Vacuum, Surfaces, and Films*, vol. 21, no. 5, pp. S74–S87, 2003, doi: 10.1116/1.1600450.

[74] Dr. O. Meyer, *Sputtering by particle bombardment, vol. I: Physical sputtering of single-elements solids*, vol. 107, no. 2–3. 1982. doi: 10.1016/0022-3115(82)90441-x.

[75] J. K. HIRVONEN, "Introduction," vol. 18, pp. 1–16, Jan. 1980, doi: 10.1016/B978-0-12-341818-0.50007-3.

[76] B. Chapman, "[박막플라즈마공정-교재] Glow Discharge Processes."

[77] "Chapter 2 Physics of sputtering," *Thin Films*, vol. 26, no. C, pp. 23–49, Jan. 1999, doi: 10.1016/S1079-4050(99)80005-2.

[78] P. D. Davidse, "Theory and practice of RF sputtering," *Vacuum*, vol. 17, no. 3, pp. 139–145, Mar. 1967, doi: 10.1016/0042-207X(67)93142-9.

[79] P. D. Davidse and L. I. Maissel, "Dielectric Thin Films through rf Sputtering," *J Appl Phys*, vol. 37, no. 2, pp. 574–579, Feb. 1966, doi: 10.1063/1.1708218.

[80] R. Surmenev *et al.*, "Radio Frequency Magnetron Sputter Deposition as a Tool for Surface Modification of Medical Implants," *Modern Technologies for Creating the Thin-film Systems and Coatings*, 2017, doi: 10.5772/66396.

[81] K. Strijckmans, R. Schelfhout, and D. Depla, "Tutorial: Hysteresis during the reactive magnetron sputtering process," *J Appl Phys*, vol. 124, no. 24, p. 241101, Dec. 2018, doi: 10.1063/1.5042084.

[82] P. Kelly, "Continual development keeps reactive sputter deposition at the forefront of surface engineering processes," *Materials Technology*, vol. 26, no. 1, pp. 1–2, 2011, doi: 10.1179/175355511X12955247420178.

[83] I. Safi, "Recent aspects concerning DC reactive magnetron sputtering of thin films: a review," *Surf Coat Technol*, vol. 127, no. 2–3, pp. 203–218, May 2000, doi: 10.1016/S0257-8972(00)00566-1.

[84] H. Blom, T. Larsson, S. Berg, and M. Östling, "Reactively sputtered titanium boride thin films," *Journal of Vacuum Science & Technology A: Vacuum, Surfaces, and Films*, vol. 7, no. 2, pp. 162–165, Mar. 1989, doi: 10.1116/1.575746.

[85] T. Zehnder and J. Patscheider, "Nanocomposite TiC/a–C:H hard coatings deposited by reactive PVD," *Surf Coat Technol*, vol. 133–134, no. 134, pp. 138–144, Nov. 2000, doi: 10.1016/S0257-8972(00)00888-4.

[86] R. Hippler, M. Cada, and Z. Hubicka, "Time-resolved Langmuir probe diagnostics of a bipolar high power impulse magnetron sputtering discharge," *Appl Phys Lett*, vol. 116, no. 6, p. 064101, Feb. 2020, doi: 10.1063/1.5140650.

[87] J. A. Thornton, D. G. Cornog, R. B. Hall, S. P. Shea, and J. D. Meakin, "Reactive sputtered copper indium diselenide films for photovoltaic applications," *Journal of Vacuum Science & Technology A: Vacuum, Surfaces, and Films*, vol. 2, no. 2, pp. 307–311, Apr. 1984, doi: 10.1116/1.572589.

[88] J. T. Gudmundsson, "Physics and technology of magnetron sputtering discharges," *Plasma Sources Sci Technol*, vol. 29, no. 11, 2020, doi: 10.1088/1361-6595/abb7bd.

[89] R. F. Bunshah and A. C. Raghuram, "Activated Reactive Evaporation Process for High Rate Deposition of Compounds," *Journal of Vacuum Science and Technology*, vol. 9, no. 6, pp. 1385–1388, Nov. 1972, doi: 10.1116/1.1317045.

[90] W. Water and S. Y. Chu, "Physical and structural properties of ZnO sputtered films," *Mater Lett*, vol. 55, no. 1–2, pp. 67–72, Jul. 2002, doi: 10.1016/S0167-577X(01)00621-8.

[91] E. M. Bachari, S. ben Amor, G. Baud, and M. Jacquet, "Photoprotective zinc oxide coatings on polyethylene terephthalate films," *Mater Sci Eng B Solid State Mater Adv Technol*, vol. 79, no. 2, pp. 165–174, 2001, doi: 10.1016/S0921-5107(00)00663-2.

[92] B. A. Movchan and A. V. Demchishin, "Structure and properties of thick condensates of nickel, titanium, tungsten, aluminum oxides and zirconium dioxide in vacuum," *The Physics of Metals and Metallography*, vol. 28. pp. 653–60, 1969.

[93] R. Messier, A. P. Giri, and R. A. Roy, "Revised structure zone model for thin film physical structure," *Journal of Vacuum Science & Technology A: Vacuum, Surfaces, and Films*, vol. 2, no. 2, pp. 500–503, 1984, doi: 10.1116/1.572604.

[94] C. R. M. Grovenor, H. T. G. Hentzell, and D. A. Smith, "The development of grain structure during growth of metallic films," *Acta Metallurgica*, vol. 32, no. 5, pp. 773–781, May 1984, doi: 10.1016/0001-6160(84)90150-0.

[95] "Sculptured Thin Films: Nanoengineered Morphology and Optics - Akhlesh Lakhtakia, R. Messier - Google Books." https://books.google.com.tr/books?hl=en&lr=&id=yCzDND-vIhMC&oi=fnd&pg=PR13&dq=sculptured+thin+films+nanoengineered+morphology+and+optics&ots=0jXKBNVZ7W&sig=oriEK365wc-RtDyypiLH-2XxQlM&redir_esc=y#v=onepage&q=sculptured%20thin%20films%20nanoengineered%20morphology%20and%20optics&f=false (accessed Dec. 06, 2022).

[96] "[Ohring_M."

[97] "10 interesting things about air – Climate Change: Vital Signs of the Planet." https://climate.nasa.gov/news/2491/10-interesting-things-about-air/ (accessed Nov. 29, 2022).

[98] A. Richter, "Weitere empfehlenswerte Titel," *Schlüsselkompetenzen spielend trainieren*, pp. 12–15, 2014.

[99] N. Illyaskutty *et al.*, "Alteration of architecture of MoO 3 nanostructures on arbitrary substrates: growth kinetics, spectroscopic and gas sensing properties," *Nanoscale*, vol. 6, no. 22, pp. 13882–13894, Oct. 2014, doi: 10.1039/C4NR04529G.

[100] M. Cich, K. Kim, H. Choi, and S. T. Hwang, "Deposition of (Zn, Mn)2SiO4 for plasma display panels using charged liquid cluster beam," *Appl Phys Lett*, vol. 73, no. 15, p. 2116, Oct. 1998, doi: 10.1063/1.122396.

[101] X. Hu, D. Ma, L. Xu, Y. Zhu, and Y. Qian, "Selective Preparation of MoO 3 and H $_x$ MoO 3 Nanobelts in Molybdenum–Hydrogen Peroxide System," *Chem Lett*, vol. 35, no. 8, pp. 962–963, Aug. 2006, doi: 10.1246/cl.2006.962.

[102] M. Itoh, K. Hayakawa, and S. Oishi, "Optical properties and electronic structures of layered MoO 3 single crystals," *Journal of Physics: Condensed Matter*, vol. 13, no. 31, pp. 6853–6864, Aug. 2001, doi: 10.1088/0953-8984/13/31/319.

[103] M. Dieterle, G. Weinberg, and G. Mestl, "Raman spectroscopy of molybdenum oxides - Part I. Structural characterization of oxygen defects in MoO3-x by DR UV/VIS, Raman spectroscopy and X-ray diffraction," *Physical Chemistry Chemical Physics*, vol. 4, no. 5, pp. 812–821, 2002, doi: 10.1039/b107012f.

[104] "Paramagnetic defects in MoO Èrevisited," pp. 5385–5392, 1999.

[105] "Paramagnetic defects in MoO Èrevisited," pp. 5385–5392, 1999.

[106] G. Mestl, N. F. D. Verbruggen, and H. Knözinger, "Mechanically Activated M0O3. 2. Characterization of Defect Structures," *Langmuir*, vol. 11, no. 8, pp. 3035–3041, 1995, doi: 10.1021/la00008a031.

[107] S. S. Sunu, E. Prabhu, V. Jayaraman, K. I. Gnanasekar, T. K. Seshagiri, and T. Gnanasekaran, "Electrical conductivity and gas sensing properties of MoO3,"

Sens Actuators B Chem, vol. 101, no. 1–2, pp. 161–174, Jun. 2004, doi: 10.1016/J.SNB.2004.02.048.

[108] M. Heinrich, S. Kluska, S. Binder, Z. Hameiri, B. Hoex, and A. G. Aberle, "Accurate potential drop sheet resistance measurements of laser-doped areas in semiconductors," *J Appl Phys*, vol. 116, no. 13, p. 134505, Oct. 2014, doi: 10.1063/1.4895584.

[109] D. H. Petersen *et al.*, "Comparative study of size dependent four-point probe sheet resistance measurement on laser annealed ultra-shallow junctions," *Journal of Vacuum Science & Technology B: Microelectronics and Nanometer Structures*, vol. 26, no. 1, p. 362, 2008, doi: 10.1116/1.2794743.

[110] N. Bowler, "Four-point potential drop measurements for materials characterization," *Meas Sci Technol*, vol. 22, no. 1, p. 012001, Jan. 2011, doi: 10.1088/0957-0233/22/1/012001.

[111] "Semiconductor Material and Device Characterization - Dieter K. Schroder - Google Books." https://books.google.com.tr/books?hl=en&lr=&id=EmozDwAAQBAJ&oi=fnd&pg=PR13&dq=D.+K.+Schroder,+Semiconductor+Material+and+Device+Characterization,+3rd+ed.+(John+Wiley+%26+Sons,+Hoboken,+NJ,+2006).&ots=YeRXeO_f6O&sig=WW0_MdQv1_IHY2V3pzWVpjijqD4&redir_esc=y#v=onepage&q&f=false (accessed Dec. 04, 2022).